USING UNSUPERVISED MACHINE LEARNING TO REDUCE THE ENERGY REQUIREMENTS OF ACTIVE FLOW CONTROL

A dissertation submitted in partial fulfillment of the
requirements for the degree of
Doctor of Philosophy

by

JARED N. KERESTES

M.S.M.E, Wright State University, 2021

B.S.M.E., Wright State University, 2020

2024

Wright State University

WRIGHT STATE UNIVERSITY
COLLEGE OF GRADUATE PROGRAMS AND HONORS STUDIES

4-19-24

I HEREBY RECOMMEND THAT THE DISSERTATION PREPARED UNDER MY SUPERVISION BY Jared N. Kerestes ENTITLED Using Unsupervised Machine Learning to Reduce the Energy Requirements of Flow Control BE ACCEPTED IN PARTIAL FULFILLMENT OF THE REQUIREMENTS FOR THE DEGREE OF Doctor of Philosophy.

_____
Mitch Wolff, Ph.D.
Dissertation Director

_____
Sherif M Elbasiouny, Ph.D.
Program Director, Ph.D. in Engineering

_____
Paula Bubulya, Ph.D.
Interim Dean, College of
Graduate Programs & Honors Studies

Committee on Final Examination:

_____
Mitch Wolff, Ph.D.

_____
Chris Marks, Ph.D.

_____
John Clark, Ph.D.

_____
George Huang, Ph.D.

ABSTRACT

Kerestes, Jared, N., Ph.D., Engineering Ph.D. Program, Department of Mechanical and Materials Engineering, Wright State University, 2024. Using Unsupervised Machine Learning to Reduce the Energy Requirements of Active Flow Control.

It is generally accepted that there exist two types of laminar separation bubbles (LSBs): short and long. The process by which a short LSB transitions to a long LSB is known as bursting. In this research, large eddy simulations (LES) are used to study the evolution of an LSB that develops along the suction surface of the L3FHW-LS at low Reynolds numbers. The L3FHW-LS is a new high-lift, high-work low-pressure turbine (LPT) blade designed at the Air Force Research Laboratory. The LSB is shown to burst over a critical range of Reynolds numbers. Bursting is discussed at length and its effect on transition, vortex shedding, and profile loss development are analyzed in depth. The results of these analyses make one point very clear: the effects of bursting are non-trivial. That is, long LSBs are not just *longer* versions of short LSBs. They are phenomena unto themselves, distinct from short LSBs in terms of their vortex dynamics, profile loss footprint, time-averaged topology, etc. This work culminates in a demonstration of how, with the aid of unsupervised machine learning, these differences can be leveraged to reduce the energy requirements of steady vortex generator jets (VGJs). Relative to pulsed VGJs, steady VGJs require significantly more energy to be effective but are more realistic to implement in actual application. By tailoring VGJ actuation to LSB type (i.e., actuating

differently in response to a long LSB than to a short LSB), it is shown that significant energy savings can be realized.

Table of Contents

List of Figures

List of Tables

Nomenclature

Latin

B	Blowing ratio
C_f	Skin friction coefficient
C_p	Pressure coefficient
C_x	Axial chord
$f_\Phi(\xi_1 \rightarrow \xi_2)$	Viscous loss fraction
$f_\epsilon(\xi_1 \rightarrow \xi_2)$	Mixing loss fraction
$f(\xi_1 \rightarrow \xi_2)$	Total loss fraction
G	Rate of total profile loss generation
G_Φ	Rate of profile loss generation due to viscous dissipation
G_ϵ	Rate of profile loss generation due to mixing
h	Height of separation bubble
h_d	Height of mean dividing streamline
H	Shape factor
l	Length of separation bubble
L_{ss}	Length of suction surface
m	Fuzziness parameter (fuzzifier)
M	Mass ratio
M_A	Cutoff mass ratio for strategy A
M_B	Cutoff mass ratio for strategy B
p	Pressure
$P(\mathrm{long})$	Probability separation bubble is long
$P(\mathrm{short})$	Probability separation bubble is short
P_0	Pohlhausen parameter
P_{Diwan}	Pressure gradient parameter due to Diwan
P_{Gaster}	Pressure gradient parameter due to Gaster
U	Velocity magnitude
u_x	Axial velocity
u_y	Pitchwise velocity
u_ξ	Streamwise component of velocity
u_η	Wall-normal component of velocity
x	Axial coordinate
y	Pitchwise coordinate

Greek

γ	Intermittency
Γ	Intermittency function

δ	Boundary layer thickness
δ^*	Boundary layer displacement thickness
ϵ	Turbulent dissipation
$\zeta_\Phi(\xi,\eta)$	Two-dimensional viscous loss distribution function
$\zeta_\epsilon(\xi,\eta)$	Two-dimensional mixing loss distribution function
$\zeta_\Phi(\xi)$	One-dimensional viscous loss distribution function
$\zeta_\epsilon(\xi)$	One-dimensional mixing loss distribution function
Z	Total profile loss
η	Wall-normal direction
θ	Boundary layer momentum thickness
λ	Fractional distance along LSB
μ	Dynamic viscosity
ν	Kinematic viscosity
ξ	Streamwise coordinate
ρ	Density
σ	Deviation from design loading
τ_{ij}	Viscous stress tensor
T	Throughflow period
ω_c	Vortex core vorticity
ω_z	Spanwise vorticity

Subscripts

0	Stagnation
1	Domain inlet
2	Domain exit
R	Reattachment
S	Separation
t	Transition onset
T	Transition completion

Acknowledgements

First and foremost, I would like to thank my family, specifically my mother and father. Without their tireless support over these many long years, I would not be where I am today. Next, I would like to thank my long-time advisor, Dr. Mitch Wolff, who supported me throughout both my master's and PhD work. It was a pleasure working with you. Many, many thanks are also due to Dr. Chris Marks who was never too busy to answer a question or offer advice. He was nothing but supportive throughout this entire process. I would also like to thank Dr. John Clark for both his help and encouragement over these past few years. Rest assured, I will never misspell *Pack-B* again.

I would also like to thank my coworkers Molly Donovan, Nathan Fletcher, and Vince Sheeler who made this process more bearable. To Molly and Nathan in particular, I have this to say: it was not a chicken platter. I feel I would be remiss if I did not also thank Dr. James Menart, with whom I took no less than 9 classes. I can honestly say, I enjoyed every one of them. I would also like to thank Dr. George Huang. It was in his computational methods class that I found my love for all things computational. Lastly, I would like to thank ADS CFD Inc., especially Michael and Bob Ni. Despite running a company, they always managed to find time to answer my many, many emails.

This material is based upon work supported by the Air Force Office of Scientific Research under award number 24RQCOR003. Any opinions, finding, and conclusions or recommendations expressed in this material are those of the author(s) and do not necessarily reflect the views of the United States Air Force.

Chapter 1: Introduction

1.1 Motivation

Over the course of a century, GTE design has matured to such a state that further gains in efficiency are increasingly difficult to obtain through improved design alone [1]. This is especially true of the low-pressure turbine (LPT). The efficiency of modern LPTs is over 90% [1]. Consequently, recent research has been directed toward reducing the weight of LPTs (among other parameters), rather than improving their efficiency through design [2].

Unlike high-pressure turbines, which typically consist of a single stage, LPTs frequently consist of 3-5 stages [3]. Consequently, LPTs contribute significantly to the weight of an engine. By one estimate, the LPT alone can account for up to one-third of the weight of an engine [4]. Aside from the obvious benefits (e.g., increased cargo capacity), decreasing the weight of an LPT also has the potential to substantially lower the life cycle cost of an engine [5]. As discussed by Schmitz et al. [2], it is possible to reduce the weight of an LPT by increasing the aerodynamic load per airfoil and/or increasing the work output per stage.

High-lift high-work airfoils aim to increase both the work output per stage and loading per airfoil. However, increasing airfoil loading, while maintaining high efficiency, presents significant design challenges. It is well known that the performance of LPTs can (and usually does) decrease with Reynolds number. This phenomenon is known as

"Reynolds lapse" and, according to Clark et al. [6], is "associated with separation of the boundary layer from turbine surfaces as atmospheric density decreases with altitude." While LPTs operate with an overall favorable pressure gradient, the suction surface (SS) curvature of the LPT blades creates localized regions of adverse pressure gradient which can lead to boundary layer separation at low Reynolds number (i.e., cruise) conditions. This problem is more acute for high-lift high-work airfoils since increasing loading tends to increase the strength of the adverse pressure gradient on the SS of the airfoils.

During cruise, the operating Reynolds number of the LPT is exceedingly low—by some estimates, as low as 25,000 (based on inlet conditions and axial chord length) [7]. At such low Reynolds numbers, the boundary layers on the airfoils of the LPT can be largely laminar, making them highly susceptible to separation [8]. When a laminar boundary layer separates, it may or may not reattach. In either case, loss increases as a result. Given the benefits of high-lift high-work airfoils, there will always exist an impetus to push loading to even higher levels. There will also always exist a loading limit beyond which separation will occur [9]. However, as discussed in Bons et al. [10], by integrating flow control into high-lift high-work airfoils, it may be possible to increase this limit.

1.2 LPTs and Flow Control

In this research, the term *flow control* is used to refer to "any mechanism or process through which the boundary layer of a fluid flow is caused to behave differently than it normally would were the flow developing naturally along a smooth straight surface" [11]. This is a narrow definition; however, for the purposes of this research, it is most suitable.

Flow control methods can be broadly classified according to whether or not they require energy input. Active flow control (AFC) requires energy input whereas passive flow control does not require energy input [12]. While relatively simple, passive methods are not adaptable and, as a result, typically incur penalties—usually in the form of parasitic drag—when not needed. Active methods are adaptable, which obviates any such penalties but require energy input and introduce additional complexity and weight. There exists a diversity of both passive and active methods for controlling boundary layer separation on the SS of LPT airfoils. Of all such methods, this research considers only vortex generator jets (VGJs).

VGJs are an active method in which jets, blown through small holes in a solid surface, are used to promote boundary layer reattachment through enhanced mixing [13]. VGJs are pitched at an angle to the surface (pitch angle) and skewed relative to the main flow direction (skew angle) as depicted Fig. 1-1.

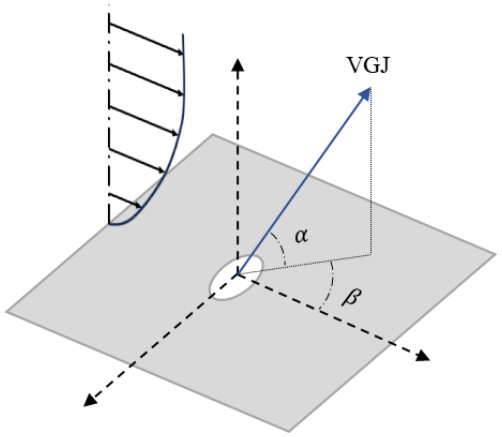

Fig. 1-1: Schematic of a VGJ depicting skew angle β and pitch angle α

VGJs are typically configured with a low pitch angle and an aggressive skew angle [3,7]. While only one VGJ is depicted in, they are typically configured in an array, much like ordinary vortex generators [13].

At this point, it is important to note that VGJs can be operated in either a pulsed or steady manner. While pulsed VGJs may be considered in the future, only steady VGJs are considered at present. Thus, the ensuing discussion on the flow physics of VGJs is only for steady operation. For a discussion of the flow physics associated with pulsed VGJs, see Bons et al. [14] or Postl et al. [15].

As described by Bons et al. [3] [10], each VGJ creates a horseshoe vortex pair with one very strong leg accompanied by a weak leg of opposite sign. With adequate skew, the two legs eventually collapse. The result is a single-sign vortex that energizes the separating boundary layer by bringing high-momentum fluid down near the wall. In this manner, the momentum necessary to energize the boundary layer is effectively "borrowed" from the freestream. By comparison, an ordinary vortex generator (or a VJG with no skew) produces two relatively weak counter-rotating horseshoe vortices. While the flow topologies produced by each device are different, both vortex generators and VGJs work to suppress separation by promoting mixing. However, relative to vortex generators, VGJs offer one very important benefit: they are adaptable. The adaptability of VGJs comes in the form of an adjustable blowing ratio, B:

$$B = (\rho U)_{\text{jet}}/(\rho U)_{\text{local}} \tag{1-1}$$

Alternatively, the mass flow rate of a VGJ may be directly specified using the mass ratio:

$$M = \dot{m}_{\text{jet}}/\dot{m}_1 \tag{1-2}$$

Relative to similar methods, namely slot blowing, VGJs require significantly less mass because VGJ holes can be spaced 10 diameters or more apart [3]. Unlike slot blowing, which generates nominally two-dimensional flow, VGJs generate highly three-dimensional flow. According to Bons et al. [3], this three-dimensional flow "creates a rapid merger of

the high-momentum fluid entrained by the individual vortices until the entire span is affected (despite the large jet spacing).” The reduced mass flow requirements of VGJs makes them an attractive option for controlling boundary layer separation in LPT applications. Moreover, the technology for implementing VGJs likely already exists [16]. Since VGJ holes have approximately the same dimensions and mass flow rates as film cooling holes, bleed air could be made available to the LPT in much the same manner that cooling air is made available to the HPT [16].

The study of Bons et al. [7] was one of the first recorded instances of VGJs being applied to the SS of an LPT airfoil. In their study of the Pratt & Whitney Pack-B airfoil, they showed, for both low (1%) and moderate (4%) levels of freestream turbulence, the VGJs drastically reduced the extent of the SS boundary layer separation. Above a minimum blowing ratio of 0.6, the wake momentum deficit was reduced by as much as 65%. The minimum effective blowing ratio was identified from a parametric study. Since the pioneering work of Bons et al. [7], many others have applied VGJs to LPT airfoils, such as Sondergaard et al. [16] and McQuilling and Jacob [17].

Similar to Bons et al. [7], Sondergaard et al. [16] applied VGJs to the suction surface of the Pack-B. They reported that, for low freestream turbulence levels (1%), the VGJs were effective at reducing total pressure loss. The loss reductions were more modest for moderate freestream turbulence levels (4%). Of the injection locations considered, the VGJs were found to be most effective when placed just upstream of separation. For both low and moderate freestream turbulence levels, an optimum blowing ratio of 1.5 was identified by means of a parametric study. Sondergaard et al. [18] later showed that, with

VGJs, it was possible to increase the design pitch spacing of the Pack-B by 50% without any appreciable increase in the per-pitch wake total pressure loss.

McQuilling and Jacob [17] experimentally investigated the effect of injection location on VGJ effectiveness for the Pack-B airfoil. They considered two different injection locations and a range of blowing ratios. Placing the VGJs at 69% SS length proved highly effective for all blowing ratios whereas placing the VGJs at 10.5% SS length proved largely ineffective. At 69% SS length, the VGJs were located within the separated region relatively close to the separation location. This supports the conclusions of Sondergaard et al. [16].

1.3 Machine Learning: A New Frontier in Flow Control

The field of fluid mechanics is quickly becoming data rich [19]. Consequently, scientific inquiry is shifting from first principles to data-driven approaches, such as machine learning. Brunton et al. [20] defines machine learning as "a rapidly developing field of computer science whereby a complex system may be learned from observational data, rather than first principles." In the context of flow control, machine learning offers the benefit of being "model-free". Traditional approaches to flow control typically involve developing feedback control laws from system models (i.e., low-order dynamical models). However, by applying actuation, the behavior of the flow often changes which, in turn, leads to a change in the fidelity of the system model [20]. Model-free approaches, as the name implies, do not require any such underlying models and, therefore, do not suffer from the same limitations.

Of the various forms of machine learning, artificial neural networks (henceforth, simply neural networks) have undoubtedly received the most attention. The study of Lee et al. [21] is one of the first recorded instances of a neural network being used for flow control. The goal of their study was to minimize the skin friction of a turbulent boundary layer using wall actuations (in the form of wall-normal blowing and/or suction) determined from a series of wall shear measurements. They elected to use a neural network to map wall shear to wall actuation (i.e., as a controller) since an exact relationship between the two could not be derived from first principles. Using this approach, they achieved drag reductions of about 20%. Their key insight was that a neural network could be used to "obtain complicated, nonlinear correlations without *a priori* knowledge of the system that is to be controlled." Since the pioneering work of Lee et al. [21], many others have used neural networks for flow control. One such germane example is the work of Brehm et al. [22] who demonstrated that a neural network could be used to make real-time predictions of the L1M flow field.

This research considers a different form of machine learning: clustering. Clustering is fundamentally different from neural networks in that it is an unsupervised machine learning technique rather than a supervised machine learning technique. The difference between supervised and unsupervised learning techniques lies in how they are trained. In training, supervised techniques require labeled input-output data, whereas unsupervised techniques do not [23]. Clustering has not been used as extensively for flow control as neural networks. Nonetheless, existing works suggest that it can be just as effective. For example, Kaiser et al. [24] demonstrated that a cluster-based control strategy was effective at reducing the mean recirculation region behind a smooth ramp. Their research stemmed

from Kaiser et at. [25] which showed that clustering constituted a potential alternative to proper orthogonal decomposition (POD) models and could therefore form the basis for a closed-loop controller. In a more recent study, Nair et al. [26] demonstrated that a cluster-based controller was effective at minimizing in-flight power consumption in post-stall flows.

1.4 Laminar Separation Bubbles

It is a well-known fact that there exist two types of laminar separation bubbles (LSB): long LSBs and short LSBs. The structures of a time-averaged short LSB and a time-averaged long LSB are depicted in Fig. 1-2.

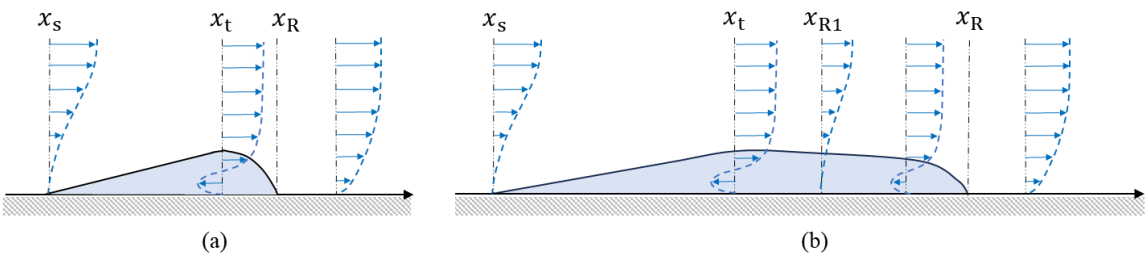

Fig. 1-2: (a) Schematic of short LSB showing (in order) separation point, transition start, and reattachment point (b) Schematic of long LSB showing (in order) separation point, transition start, 'reattachment-like' behavior, and reattachment point

What follows is a simplified description of the flow topologies associated with each bubble type. The descriptions follow closely those of Hatman and Wang [27]. For short LSBs, the onset of transition (x_t) is observed to take place downstream of separation (x_S), near the location of the maximum displacement of the shear layer. The high rate of turbulence production and the ejection-shedding process entrain sufficient momentum to force the separated shear layer to reattach (x_R). The final coalescence into turbulence (x_T) takes

place in the reattaching boundary layer. Some distance downstream of reattachment, a fully developed turbulent boundary layer profile is recovered.

For a long bubble, the onset of transition is also observed to coincide with the location of the maximum displacement of the shear layer. The increased mixing in the region of the maximum displacement of the shear layer (x_{MD}) leads to the first 'reattachment-like' behavior (x_{R1}). However, relative to short LSBs the mixing is weaker, and the shear layer fails to remain attached. The final coalescence into turbulence occurs further downstream, somewhere between x_{MD} and x_T, and forces the shear layer to reattach. Again, a fully developed turbulent boundary layer profile is recovered sufficiently far downstream.

The process by which a short bubble transitions to a long bubble has been described in the literature as "bursting." What follows is a review of classical bursting models. Such models attempt to predict the onset of bursting using time-averaged quantities. Since bursting is typically associated with a rapid increase in the length and height (thickness) of a separation bubble, Owen and Klanfer [28] originally classified LSBs on the basis of their length l. For short bubbles, they claimed $l/\delta_S^* = O(10^2)$ while for long bubbles they claimed $l/\delta_S^* = O(10^4)$. Here δ_S^* is the boundary layer displacement thickness at separation. As later research has shown, the distinction between the two types of bubbles is not so clear; while bursting is always accompanied by an increase in l, this increase may not always be as marked as Owen and Klanfer suggest [29].

This lead Tani [30] to classify the two types of bubbles based on their effect on the time-averaged pressure distribution. According to Tani, a short separation bubble has a slight effect on the pressure distribution. The pressure distribution departs from its

theoretical (i.e., inviscid) form only in the vicinity of the bubble. While short LSBs may also slightly reduce the magnitude of the suction peak ahead of separation, their effects are largely local. A long LSB, on the other hand, significantly modifies the pressure distribution. So much so, that the suction peak 'collapses' to a lower value and the constant pressure plateau after separation is larger and at a higher pressure.

Over the years, many criteria have been proposed to predict bursting. The criterion due to Gaster [31] is perhaps the most famous. Based on dimensional analysis, Gaster argued that the structure of an LSB depends on two parameters. The first is a nondimensional pressure gradient parameter:

$$P_{\text{Gaster}} = \left(\frac{\theta_{\text{S}}^2}{\nu}\right)\frac{(\Delta U)_{\text{inviscid}}}{l} \tag{1-3}$$

The second is the momentum thickness Reynolds number at separation $Re_{\theta,s}$. In Eq. (1-3)(2-8) θ_s is the momentum thickness at separation, ν is the kinematic viscosity, and ΔU is the velocity change across L for the ideal (i.e., inviscid) case. From an analysis of experimental data, Gaster identified a curve (which he referred to as the 'bursting line') in the $P_{\text{Gaster}} - Re_{\theta,s}$ plane that he claimed separated short LSBs from long LSBs. Gaster's original diagram is reproduced in Fig. 1-3.

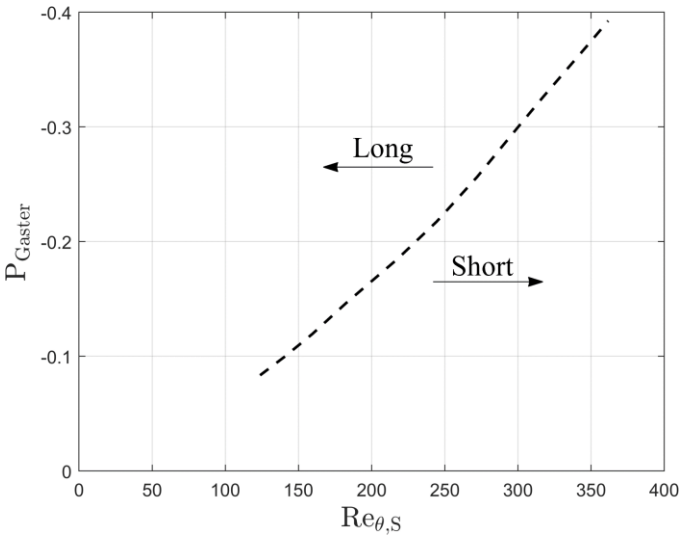

Fig. 1-3: Bursting diagram of Gaster [31]

Points lying to the right of the bursting line correspond to short LSBs. Similarly, points lying to the left of the bursting line correspond to long LSBs.

While celebrated, Gaster's bursting criterion is not universal. There are a number of instances in which it incorrectly classifies LSBs (see, for example, Mitra et al. [32]). Based on Gaster's work, Diwan et al. [33] proposed a similar criterion. Instead of using momentum thickness at separation as their length scale, they chose to use the height of the LSB (h) since "the local conditions at the streamwise location of maximum height of the bubble can be expected to influence the approach of the separated shear layer towards reattachment." Moreover, they chose to use the actual change in velocity across L rather than the ideal change. The pressure gradient parameter of Diwan et al. [33] can be written as

$$P_{\text{Diwan}} = \left(\frac{h^2}{\nu}\right)\frac{(\Delta U)_{\text{actual}}}{l} \tag{1-4}$$

From an analysis of many experimental data sets, they arrived at a much simpler bursting criterion that, unlike the criterion of Gaster, can be expressed in closed form:

$P_{\text{Diwan}} = -28$. According to their model, $P_{\text{Diwan}} > -28$ correspond to a short bubble while $P_{\text{Diwan}} < -28$ corresponds to a long bubble. By changing the length scale, Diwan et al. [33] were able to reduce the two-parameter bursting criterion of Gaster to a single-parameter bursting criterion. The recent study of Mitra et al. [32] suggests that, despite being relatively simple, the one parameter bursting criterion of Diwan et al. [33] is rather accurate. Note that other bursting criteria have been proposed, but only the above two will be considered.

1.5 Transition and Laminar Separation Bubbles

Volino [34] said it best: "separation on LPT airfoils is complicated by boundary layer transition." According to Mayle [35], there are three modes of transition. The first mode is natural transition. In brief, natural transition begins with the formation of weak instability waves (commonly referred to as Tollmien-Schlichting waves) in the laminar boundary layer. As these waves propagate downstream, they are either amplified, if the flow is unstable to them, or attenuated. Once the amplitude of the instability waves reaches a critical threshold, the flow enters a phase of nonlinear breakdown and randomization. During this phase, the formation of turbulent spots is observed to occur. Eventually, the turbulent spots coalesce into a fully developed turbulent boundary layer completing the transition process. See Kachanov [36] for a more detailed description of the natural transition process. The second mode is bypass transition. Bypass transition occurs when external disturbances (e.g., freestream turbulence) cause the flow to 'bypass' the first few phases of natural transition. The final mode is separated-flow transition. Here, transition occurs in a separated laminar boundary layer (i.e., a free shear layer). In the absence of

significant levels of environmental disturbances (i.e., freestream turbulence), transition of a separated shear layer is initiated through the Kelvin-Helmholtz instability mechanism [37].

Of the three modes of transition, separated-flow transition is, perhaps, the most important in LPT applications [35]. This is because separated-flow transition dictates where and if a separated laminar boundary layer reattaches. If the free shear layer formed by boundary layer separation transitions sufficiently close to the separation point, it typically reattaches and forms a closed LSB (in the time-average sense); if, however, the separated shear layer does not transition sufficiently close to the separation point, it typically does not reattach [35]. This is depicted schematically in Fig. 1-4.

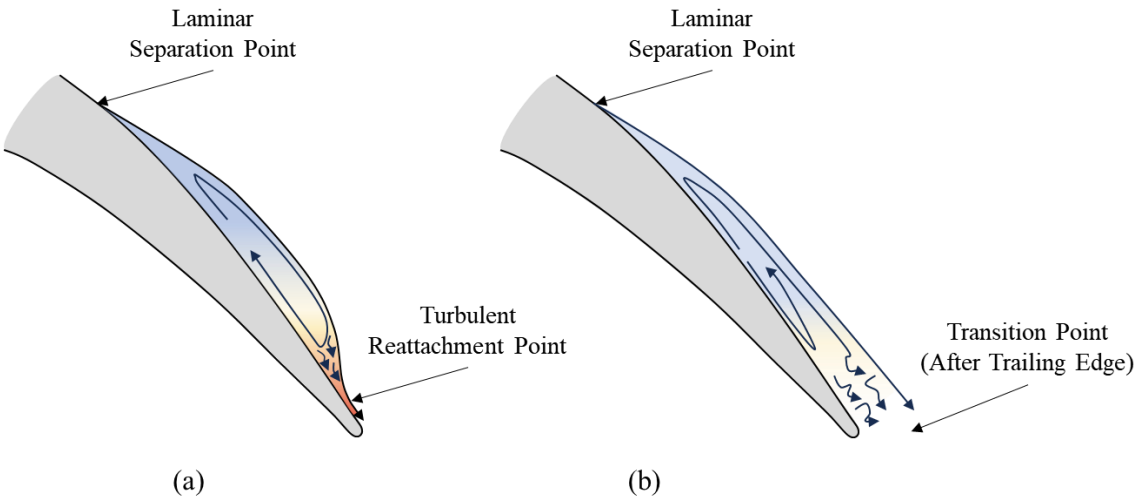

Fig. 1-4: (a) Transition occurs close to the separation point, resulting in a laminar separation bubble (b) Transition does not occur close to the separation point, resulting in open (i.e., un-reattaching) separation.

By one estimate, losses may increase by as much as 500% if the separated shear layer does not reattach [38]. Obviously, it is preferable for the shear layer to reattach.

In the event that the separated shear layer reattaches, the length of the resulting LSB depends on the location of transition. As might be expected, loss increases with increasing LSB length. This being the case, why not induce transition prematurely to shorten or, potentially, eliminate the LSB altogether? Unfortunately, it is not so simple. While moving the transition point upstream tends to decrease the length of the LSB, it also tends to increase the extent of the turbulent reattachment region [39]. Since turbulent flows are typically associated with higher frictional losses, the net result of these competing effects is not immediately obvious. According to Volino [34], "existing results suggest that separation bubbles should be kept small, but without producing an unnecessarily long turbulent region." Mayle [35] echoes this sentiment: "short bubbles are an effective way to force the flow turbulent and may be considered as a means to enhance performance." This idea has led to the concept of controlled-diffusion blading, as discussed by Hourmouziadis [40]. In controlled-diffusion blading, airfoils are designed such that a short LSB is present. Short LSBs are not thick enough to produce high losses. Moreover, relative to tripping the boundary layer upstream, short LSBs usually result in a smaller turbulent region.

1.6 The L3FHW-LS

As discussed by Clark et al. [6], a new series of high-lift high-work LPT airfoils was recently designed at the U.S. Air Force Research Laboratory. The goal of the series was to achieve exceptionally high loading and lift while also decreasing the severity of Reynolds lapse. The complete series of airfoils, designated the LXFHW series, includes rotating stages, annular cascades, and both transonic and incompressible-equivalent linear cascades. LXFHW is an acronym: L indicates an LPT airfoil, X is a wildcard representing

the mean-line loading level of the airfoil (possible values are 1-3, with 1 representing the lowest loading level and 3 representing the highest loading level), F indicates the airfoil is front-loaded, and HW indicates the airfoil is part of a high-work stage. This research concerns only one airfoil from the incompressible family: L3FHW-LS. Here, the suffix -LS is used to indicate a low-speed airfoil.

The LXFHW-LS family is a subset of the LPT geometries created at the Air Force Research Laboratory (AFRL) since 2005 to investigate the limits of the expanded design space enabled through careful consideration of the local state of the boundary layer [38,41] over the blades as they are defined. The aerodynamic characteristics of the LXFHW-LS family are summarized in Table 1-1. In Table 1-1, C_o is circulation-based formulation of the lift coefficient [42], here called the Coull number, Z_w is the familiar Zweifel loading coefficient [43], N is the number of blades in one stage, and S/C_x is the pitch (S) normalized by the axial chord (C_x).

Table 1-1: Aerodynamic characteristics of LXFHW-LS family

Airfoil	N	S/C_x	**Turning (°)**	**Loading Type**	Z_w	C_o
L1FHW-LS	72	1.016	122.1	Front	1.32	0.84
L2FHW-LS	60	1.216	123.0	Front	1.60	0.90
L3FHW-LS	54	1.376	122.5	Front	1.78	0.92

The family was designed consistent with the velocity triangles of the LPT13 high-work stage, first embodied in the ND-HiLT01 turbine [2,44]. The LPT13 represents an increase in turning of approximately 30° over the Pack-B. This is consistent with an increase in the work coefficient of approximately 40% for the airfoils of the LXFHW-LS family over

those designed to Pack B air angles. For a further discussion on the design of the family as a whole, see Clark et al. [6].

1.7 Dissertation Objectives

In a recent study, Kerestes et al. [45] investigated the low-Re performance of the L3 and found that an LSB developed over the aft part of the suction surface for $\mathrm{Re}_\infty < 160{,}000$. While the LSB grew longer with decreasing Reynolds number, they reported no indication of unreattaching boundary layer separation down to $\mathrm{Re}_\infty = 25{,}000$. The objectives of this research are to

1. show that the LSB bursts over a critical range of Reynolds numbers
2. develop a machine-learned bursting criterion and assess its ability to predict bursting
3. determine how bursting affects the time-averaged topology, vortex dynamics, and loss footprint of the separation bubble
4. demonstrate how, with the aid of a machine-learned bursting criterion, the differences between long and short LSBs might be leveraged to reduce the energy requirements of steady VGJs

Chapter 2: Approach

2.1 LES

2.1.1 General Procedure

All LES simulations were accomplished using the GPU-accelerated flow solver, Leo, from Aerodynamic Solutions (ADS). Leo is a compressible, finite-volume flow solver. It employs the Ni-Scheme distribution [46,47] that is second-order accurate in both space and time. The procedure of Ni et al. [48] was followed for all simulations. In brief, the procedure consists of 4 steps: 1) obtain a converged RANS solution, 2) initialize the LES solution from the converged RANS solution, 3) flush the transient and, 4) enable time-averaging. For a more detailed description of the LES procedure, see Ref. [48].

Reynolds number was altered by varying the inlet total pressure, $p_{0,1}$, while keeping the ratio $p_{0,1}/p_2$ constant. The pressure ratio was chosen such that the exit Mach number was $M_2 \approx 0.2$. This ensured the Mach number throughout the entire domain was greater than 0.1. Even though Leo preconditions the governing equations, it is still best to ensure the Mach number is not too low. As a general rule of thumb, "too low" it typically taken to mean < 0.1.

The time-step size (Δt) was based on the so-called convection time-step size:

$$\Delta t_c = \frac{T}{N_{\mathrm{ss}}} \tag{2-1}$$

In Eq. (2-1), T is the through-flow period

$$T = \frac{C_x}{u_{x,1}} \tag{2-2}$$

and N_{ss} is the number of grid points defining the suction surface. Δt_c is an approximate measure of the amount of time it takes a particle of fluid to travel from one grid point to the next. For all simulations, $\Delta \mathrm{t}$ was set such that $\Delta \mathrm{t} < \Delta t_c$.

Time averaging occurred for approximately $40T$ and was enabled only after the transient was flushed (step 3 above). To flush the transient, each LES simulation was integrated for $10T$. All numerical results reported later were the result of time averaging over $40T$.

2.1.2 Computational Mesh

The computational mesh was generated using the preprocessor, WAND, also from ADS. WAND generates structured, multi-block, meshes using a Poisson solver. The block topology was O-type in the near-wall region and H-type in the far-field. The computational mesh is depicted in Fig. 2-1.

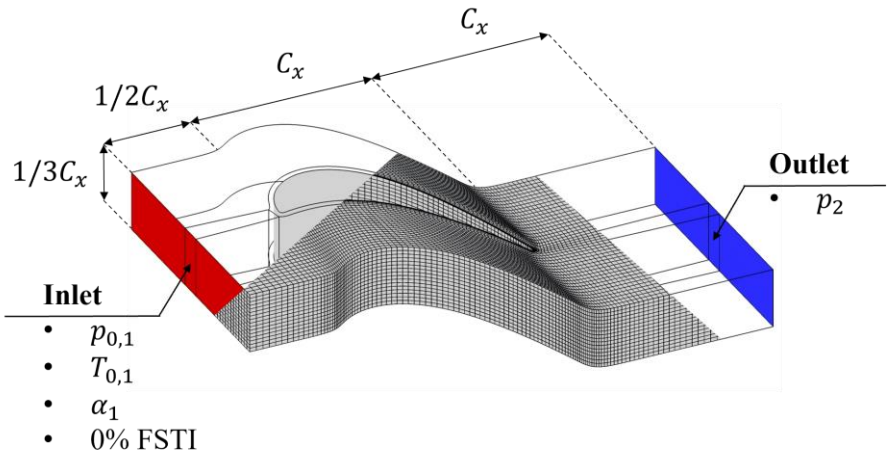

Fig. 2-1: Computational mesh (every fourth node shown) with cutaway showing the structure of the underlying block topology. The domain inlet is shaded red, and the domain outlet is shaded blue

The computational domain extended $0.5C_x$ upstream, $1C_x$ downstream, and $1/3C_x$ in the spanwise direction. The same mesh was used for all Reynolds numbers; it was sized based on the highest Reynolds number considered ($\mathrm{Re}_\infty = 100{,}000$) and consisted of approximately fourteen million hexahedral elements. In near-wall regions, the mesh was refined such that $y^+ < 1$, $x^+ \ll 150$, and $z^+ \ll 40$. This is consistent with the minimum LES grid resolution requirements recommended by Georgiadis et al. [49]. For most Reynolds numbers, the mesh resolution exceeded DNS levels as depicted in Fig. 2-2.

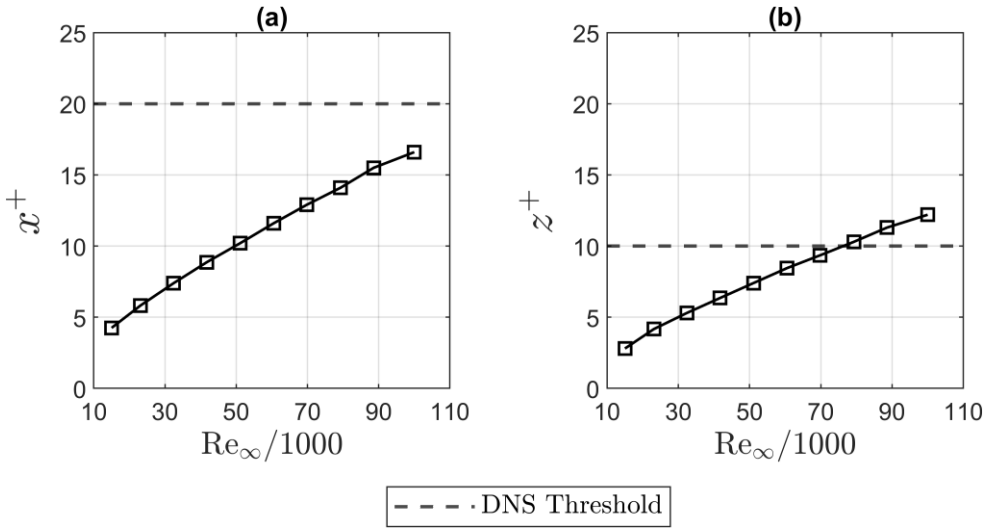

Fig. 2-2: (a) streamwise grid resolution (b) spanwise grid resolution. Dashed black line marks DNS threshold (from [49]).

To check for mesh independence, one additional simulation was conducted at $\mathrm{Re}_\infty = 100{,}000$ using a mesh approximately 50% denser than the baseline 14 million element mesh. Time-averaged integrated total pressure loss changed by <1%.

2.1.3 Boundary Conditions

Total pressure, total temperature, and flow angle were specified at the inlet boundary (highlighted red in Fig. 2-1). The flow entering the domain was perfectly uniform (i.e., the inlet freestream turbulence intensity was exactly 0%). At the exit boundary (highlighted blue in Fig. 2-1), only static pressure was specified. Flow periodicity was imposed in the pitchwise direction. The no-slip condition was imposed on the blade surface; the blade surface was also considered adiabatic. Spanwise boundaries were treated as inviscid walls. For simulations involving VGJs, the VGJs were modeled using a transpiration boundary condition.

2.2 Machine-Learned Bursting Criterion

2.2.1 A Brief Review of Clustering

While the information in this section could have been presented earlier, with the other introductory material, it makes more sense for it to be presented alongside the discussion of the machine learning model.

Abstractly, clustering is the process of grouping similar objects together [50]. From this definition, it follows that a cluster is a set of similar objects. The basic data in a clustering problem are a set of objects, each described by a set of features. For example, the data might be a set of flowers, each described by petal length, petal width, and sepal length. After clustering, if some object in a cluster has a certain feature, other objects in the cluster are expected to have the same feature [50]. Therefore, by examining objects in different clusters, it is possible to determine how they differ. More specifically, it is possible to determine what features make them different. Clustering is used extensively in the modern world, particularly in e-commerce. Most people, at some point or another, have received an ad for ‘similar products’ or ‘products you might like’ after purchasing something online. Ever wondered how this is possible? In e-commerce, it is common to cluster users into groups based on their purchasing or web-surfing history and then send targeted ads to each group [23].

As mentioned earlier, clustering is a type of unsupervised machine learning in which only input data are provided. Unlike supervised machine learning, the input data are unlabeled. The goal of clustering is to discover some “interesting structure” in the input data; hence, clustering is sometimes referred to as ‘knowledge discovery.’ Unsupervised machine learning is arguably more typical of how humans learn. Geoff Hinton once said:

> "When we're learning to see, nobody's telling us what the right answers are — we just look. Every so often, your mother says, "that's a dog", but that's very little information. You'd be lucky if you got a few bits of information — even one bit per second — that way. The brain's visual system has 10^{14} neural connections. And you only live for 10^{9} seconds. So, it's no use learning one bit per second. You need more like 10^{5} bits per second. And there's only one place you can get that much information: from the input itself" [51].

Unsupervised learning is also more widely applicable than supervised learning, as it does not require a human to manually label the data.

While fuzzy c-mean clustering (FCM) [52–54] is used in this research, the k-means algorithm [55,56] is discussed first, as it is the algorithm upon which FCM is based. Given a set of observations, the k-means algorithm groups the observations into k clusters, hence the 'k' in k-means. Each set of observations belonging to a cluster is represented by its corresponding cluster centroid, which is computed as the mean over all observations in the cluster. In the k-means algorithm, each observation can be a member of at most one cluster. That is, membership is binary. The observation either belongs to a cluster or it does not. For the present work, this is not ideal, as bursting is not an instantaneous event and takes place over a finite range of Reynolds numbers [31].

FCM is very similar to k-means, except that membership is non-binary. That is, membership is probabilistic instead of deterministic. FCM is based on fuzzy set theory which gives the concept of uncertainty in data attribution. In FCM, each observation has a probability of membership to each cluster. This is why c-means is sometimes referred to

as soft clustering. The difference between k-means and FCM clustering is illustrated in Fig. 2-3.

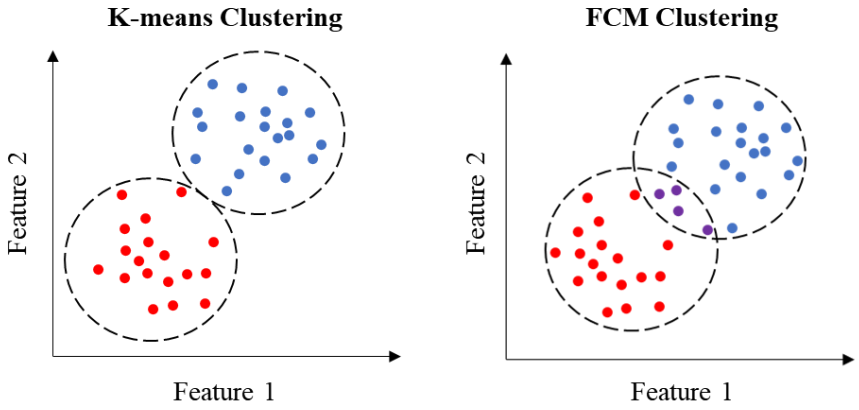

Fig. 2-3: Pictorial representation of the differences between k-means clustering and FCM clustering

In this research, the FCM algorithm is used. In brief, the classic version of the algorithm seeks to minimize the following objective function:

$$J(\boldsymbol{M}, \boldsymbol{C}) = \sum_{n=1}^{N} \sum_{k=1}^{K} \mu_{nk}^{m} d_{nk}^{2} \tag{2-3}$$

In Eq. (2-3) $\boldsymbol{M}$ is the fuzzy partition matrix, $\mathcal{C}$ is the set of all cluster centroids, N is the number of observations, K is the number of centroids, μ_{nk} is the degree of membership of the n^{th} observation to the k^{th} cluster, m is the degree of fuzzy overlap, and d_{nk} is the distance from the n^{th} observation to the k^{th} cluster. Since the goal of clustering is to minimize intra-cluster similarity and maximize inter-cluster similarity, each clustering algorithm must define a similarity metric (i.e., a means of measuring how similar two observations are). The FCM algorithm uses the distance between observations in feature space as a measure of similarity. In this work, distance is computed using the standard Euclidean norm, as called for by the classic version of the algorithm. However, other norms

(e.g., the L_1 norm) can be used. For more information on the classic FCM algorithm see Bezdek [52] or Bezdek et al. [53].

2.2.2 Design of a Cluster-Based Bursting Criterion

Short and *long* are very abstract concepts that cannot directly be measured. This is where bursting criteria come in. They attempt to define *short* and *long* in terms of quantities that *are* measurable. For example, Owen and Klanfer [28] define a short LSB as an LSB for which $l/\delta_S^* = O(10^2)$. As discussed earlier, there exist a number of bursting criteria. However, existing bursting criteria rely on quantities that are rather difficult to measure (e.g., θ or h), making them ill-suited for flow applications.

Using machine learning, it may be possible to develop a bursting criterion based on easy-to-measure quantities. According to Gross and Fasel [57], wall shear stress and wall pressure are quantities that might be realistic to measure in actual application. This work proposes to use FCM clustering, to distinguish between short and long LSBs. Unsupervised machine learning is preferred to supervised machine learning since the latter requires human-labeled data. In this instance, providing labeled data may inject unwanted bias into the model, given that there is no definitive way to distinguish short LSBs from long LSBs.

The machine learning model is trained to distinguish short LSBs from long LSBs on the basis of pressure. Since one of the major differences between short and long LSBs is their impact on peak suction, it seems most appropriate to base the model on pressure measurements taken in this neighborhood. Given three pressure measurements taken in the neighborhood of peak suction, the trained model returns the likelihood (i.e., probability) that the LSB is long and/or short.

Classic FCM has two hyperparameters (i.e., arbitrary parameters that must be specified by the user). The first is the number of clusters. Clearly, the most appropriate number of clusters is 2. One cluster for short LSBs and another for long LSBs. The second hyperparameter is the so-called *fuzzifier*, m. As the name implies, this determines how 'fuzzy' the interface is between the two clusters. m was taken to be 1.2. Note that, in the limit as m approaches 1, FCM approaches k-means. Traditionally, $m = 2$. However, a more conservative value of $m = 1.2$ was found to be more appropriate. For higher values of m, the resulting model was so fuzzy as not to be useful.

The data set upon which the machine learning model was based consisted of 400 observations, 50 from each of 8 different Reynolds numbers. The Reynolds numbers were equally spaced between $\mathrm{Re}_\infty = 15{,}000$ and $\mathrm{Re}_\infty = 100{,}000$. All observations were acquired randomly in time once the simulations had achieved a statistically steady state (i.e., after step 3 of the LES procedure). An observation consisted of three measurements: σ_I, σ_{II}, and σ_{III}. Here, σ_i is the instantaneous deviation of the loading distribution at location i from the design loading distribution at the same location. σ_i is used instead of $C_{p,i}$ to make the final model both more general and more interpretable. By using σ_i, the final model can be interpreted as a data-driven realization of the classification scheme of Tani [30]. Tani was the first to propose that LSBs be classified based on their effect on the pressure distribution. He suggested that a long LSB has a global effect on the loading distribution, whereas a short LSB has a local effect on the loading distribution. The present model quantifies this idea. Measurement locations are summarized in Table 2-1.

Table 2-1: Streamwise location of each σ_i.

Feature	Location description
σ_I	$0.05L_{ss}$ upstream of peak suction ($\xi/L_{ss} = 0.15$)
σ_{II}	Coincident with peak suction ($\xi/L_{ss} = 0.20$)
σ_{III}	$0.05L_{ss}$ downstream of peak suction ($\xi/L_{ss} = 0.25$)

In examining Table 2-1 it is apparent that the measurement locations are symmetric about the location of peak suction.

The data used for training are visualized in Fig. 2-4.

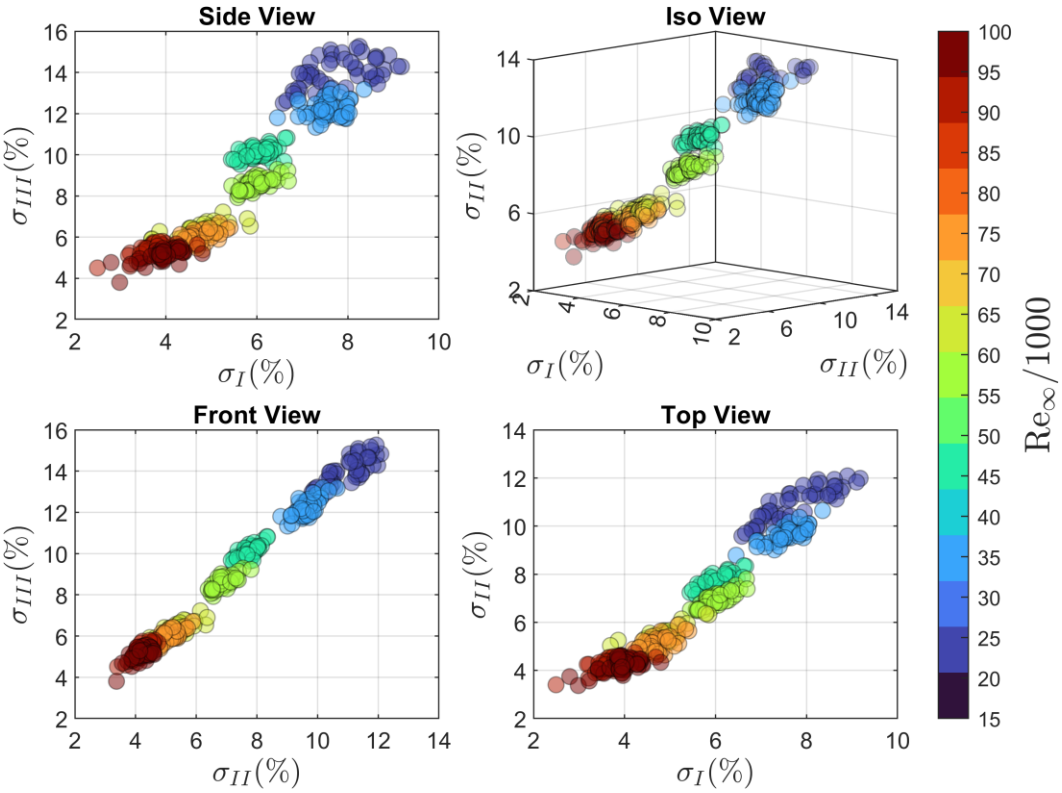

Fig. 2-4: Various views of the training data set, all of which are plotted in feature space.

The data points from the higher Reynolds numbers tend to be located near the origin. This stands to reason, as the origin corresponds to the design point. As expected, σ_I, σ_{II}, and

σ_{III} are relatively small for $\mathrm{Re}_\infty = 100{,}000$ and significantly larger for $\mathrm{Re}_\infty = 25{,}000$. In examining Fig. 2-4, it is clear that the data are strongly correlated. This suggests that the dimensionality of the feature space can be reduced by applying a dimensionality reduction technique, such as principal component analysis (PCA). According to Jolliffe [58] "the central idea of principal component analysis is to reduce the dimensionality of a data set consisting of a large number of interrelated variables, while retaining as much as possible of the variation present in the data set." PCA is an application of the singular value decomposition that provides a new set of coordinates, the so-called principal components, which are uncorrelated, and which are ordered by their significance [58,59].

To perform PCA, the present data were first centered and arranged into a matrix $\boldsymbol{X}$. The rows of $\boldsymbol{X}$ corresponded to individual observations and the columns corresponded to features. The covariance matrix $\boldsymbol{C}$

$$\boldsymbol{C} = \frac{1}{N-1}\boldsymbol{X}^T\boldsymbol{X} \tag{2-4}$$

was then constructed from $\boldsymbol{X}$. The principal components

$$\boldsymbol{T} = \boldsymbol{U}\boldsymbol{\Sigma} \tag{2-5}$$

were computed from the SVD factorization of $\boldsymbol{C}$:

$$\boldsymbol{C} = \boldsymbol{U}\boldsymbol{\Sigma}\boldsymbol{V}^{\boldsymbol{T}} \tag{2-6}$$

Here, $\boldsymbol{U}$ and $\boldsymbol{V}$ are unitary matrices, the columns of which are known as right singular vectors and left singular vectors respectively. $\boldsymbol{\Sigma}$ is a diagonal matrix, the nonzero elements of which are referred to as singular values. The data is plotted in both feature space and principal component space in Fig. 2-5. Note that, in Fig. 2-5a, the principal component axes are placed at the mean of the data set. This was done purely for visualization purposes.

When the data was actually transformed, the axes were placed at the origin. This is reflected in Fig. 2-5b, as PC1 is nonnegative.

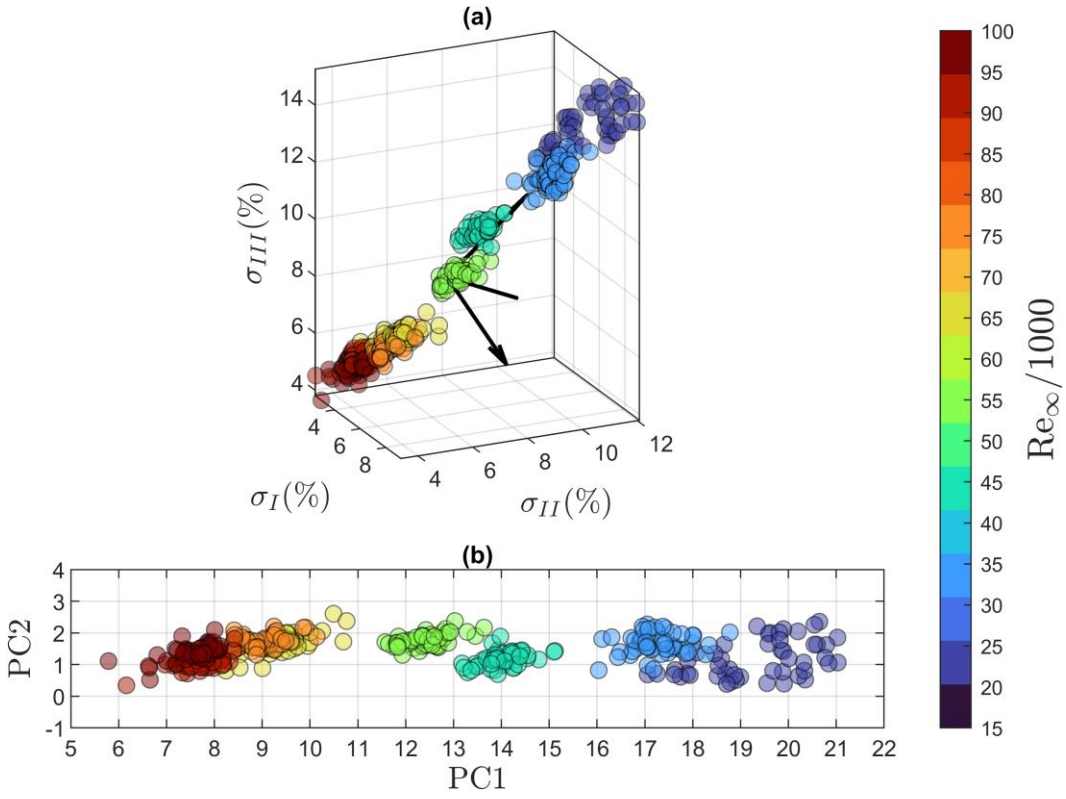

Fig. 2-5: (a) Data set plotted in feature space overlaid with principal component directions (b) Data set plotted in principal component space (only the first two components are depicted).

Interestingly, the data for $\mathrm{Re}_\infty > 60{,}000$ and $\mathrm{Re}_\infty < 40{,}000$ appear to form two distinct clusters. The data for $40{,}000 \leq \mathrm{Re}_\infty \leq 60{,}000$ exists in between these clusters. While these structures are most clearly seen in principal component space, they are also apparent in feature space. Since the training data were sampled from 8 equally spaced Reynolds numbers, these structures cannot be an artifact of the choice of Reynolds numbers.

Judging from Fig. 2-5b, it seems that PC1 is significantly more important than PC2. This is confirmed by examining the singular values. The singular value corresponding to

PC1 is over an order of magnitude larger than the singular value corresponding to PC2. Thus, PC1 explains significantly more of the variance of the data set (sometimes referred to as energy) than PC2. In point of fact, PC1 alone explains over 90% of the variance of the data set. For this reason, PC2 and PC3 are discarded. This reduces the dimensionality of the data from 3 to 1. In terms of σ_i, PC1 is given by

$$\text{PC1} = 0.347\sigma_I + 0.565\sigma_{II} + 0.749\sigma_{III} \tag{2-7}$$

Surprisingly, σ_{III} is weighted the most; it was expected that σ_{II} would be weighted the most given that it corresponds to the location of peak suction.

The machine learning model was implemented using the fuzzy logic toolbox of MATLAB. After the clustering process was complete, the probability of membership of each data point to both the *long* and *short* cluster was calculated. The result is depicted in Fig. 2-6.

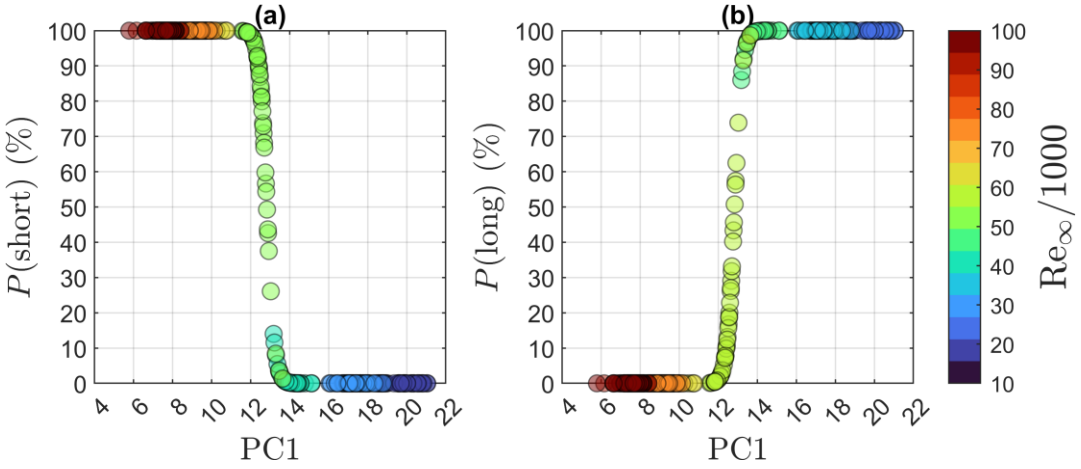

Fig. 2-6: Probability of membership of data to (a) short cluster and (b) long cluster.

The machine learning model predicts that the LSB is short for $\text{Re}_\infty > 60{,}000$ and long for $\text{Re}_\infty < 40{,}000$. This behavior is consistent with the observations made earlier regarding the natural structures apparent in the training data. According to the machine learning model, bursting occurs over the range $40{,}000 \leq \text{Re}_\infty \leq 60{,}000$, since this is the range

over which $P(\text{short})$ decreases from 100% to 0% (alternatively, it could be said that this is the range over which $P(\text{long})$ increases from 0% to 100%). The accuracy of the model will be addressed later, after the actual range over which bursting occurs has been established.

2.3 Post-Processing Techniques

2.3.1 Intermittency Analysis

The intermittency (γ) was calculated using the algorithm of Volino et al. [60]. This algorithm was chosen since it has been demonstrated to work well in LPT applications [61,62]. By definition, the intermittency is the time average of the intermittency function $\Gamma(t)$, which indicates whether a flow is instantaneously turbulent or non-turbulent at any given time (for this reason, the intermittency function is sometimes referred to as the *indicator function*). $\Gamma(t)$ takes the value 0 when the flow is nonturbulent and 1 when the flow is turbulent. The difficulty lies in determining whether a flow is instantaneously turbulent or nonturbulent.

In brief, the algorithm of Volino et al. [60], uses two detector functions to discriminate between turbulent and non-turbulent flow:

$$\mathcal{D}_1(t) = \left[\frac{\partial\left(u_x' u_y'\right)}{\partial t}\right]^2 \tag{2-8}$$

$$\mathcal{D}_2(t) = \left[\frac{\partial^2\left(u_x' u_y'\right)}{\partial t^2}\right]^2 \tag{2-9}$$

The flow is considered turbulent if $\mathcal{D}_1(t) > C_1$ or $\mathcal{D}_2(t) > C_2$, where C_1 and C_2 are arbitrary thresholds. The user specifies only C_1; C_2 is set based on C_1. See Volino et al. [60] for more information.

In this work, C_1 was set after having inspected many time traces of $\Gamma(t)$. One such time trace is shown in Fig. 2-7.

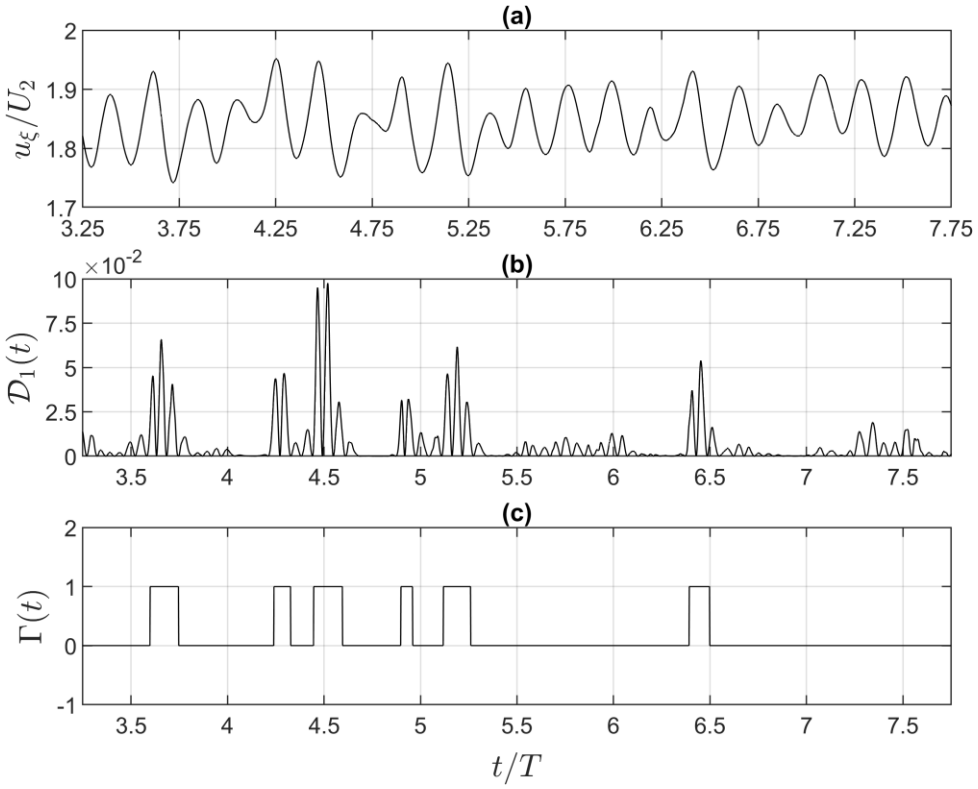

Fig. 2-7: (a) streamwise velocity (b) first detector function (b) final intermittency function; time traces taken near transition onset for $\mathrm{Re}_\infty = 15{,}000$.

For the location shown, $\Gamma(t)$ does a good job separating turbulent from non-turbulent samples. Ultimately, visual inspection is the best way to determine how well $\Gamma(t)$ is separating turbulent from non-turbulent samples [63]. For this reason, choosing C_1 is more of an art than a science.

2.3.2 Vortex Core Tracking

Vortex cores were identified using the algorithm of Jiang et al. [64] In brief, the algorithm works by visiting each point P in a velocity field and checking to see if the so-called "direction-spanning" property is satisfied in the neighborhood of P. If the direction spanning property is satisfied, P is identified as a vortex core. See Jiang et al for more information.

While the algorithm generally worked well, it tended to identify multiple cores per vortex, as illustrated in Fig. 2-8a.

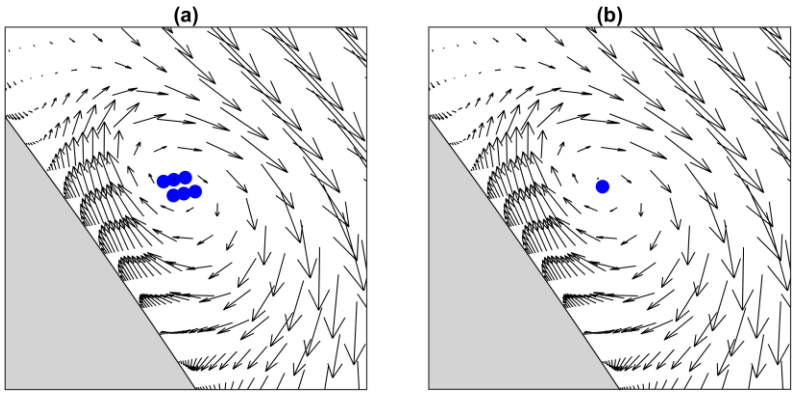

Fig. 2-8: (a) cores belonging to a single group (b) centroid of group; single timestep from $\mathrm{Re}_\infty = 15{,}000$ shown.

To correct this, an auxiliary step was added to the algorithm. After all cores had been identified, they were grouped together. To initiate this process, a group was created consisting of a random core. Then, the remaining cores were looped over. If a core was within $0.02L_{ss}$ of an existing group, it was assigned to that group. Otherwise, a new group was created. Once all cores were assigned to a group, the centroid of each group was taken to be the new location of the vortex core. A single group is depicted in Fig. 2-8a and its corresponding centroid is depicted in Fig. 2-8b. The centroid of the group is very close to the true vortex core.

2.3.3 Loss Decomposition and Analysis

This section describes an approximate method for calculating the time-averaged profile loss generated over an arbitrary region for a statistically steady flow. Broadly speaking, loss can be broken down into three components: 1) profiles loss, 2) endwall loss, and 3) leakage loss [65]. Only profile loss is of interest in this work. Profile loss is typically

regarded as the loss generated in the boundary layers of the LPT blades, well away from any endwalls [65]. Trailing edge loss is also usually included in profile loss; trailing edge loss is the colloquial name given to the loss generated by the "mixing out" of the wake behind the trailing edge.

For an incompressible, steady flow the transport of total pressure is governed by

$$\frac{\partial}{\partial x_i}(u_i p_0) = \frac{\partial u_j \tau_{ij}}{\partial x_i} - \tau_{ij}\frac{\partial u_j}{\partial x_i} \tag{2-10}$$

For a derivation of the above, see Issa [66]. Note that τ_{ij} is the stress tensor:

$$\tau_{ij} = \mu\left(\frac{\partial u_i}{\partial x_j} + \frac{\partial u_j}{\partial x_i}\right) \tag{2-11}$$

According to Eq. (2-10), two mechanisms can influence total pressure: stress work and dissipation. The first term on the right-hand side of Eq. (2-10) represents the stress work rate. The second term on the right-hand side of Eq. (2-10) represents the dissipation rate (i.e., the rate at which kinetic energy is converted into internal energy).

The majority of profile loss is generated in boundary layer regions [67]. In such regions, the velocity gradient is typically very large. While stress work scales with the velocity gradient, viscous dissipation scales with the square of the velocity gradient. Consequently, changes in total pressure due to stress work are assumed to be negligible. Therefore,

$$G = \tau_{ij}\frac{\partial u_j}{\partial x_i} \tag{2-12}$$

Here G is the generation rate of profile loss at a point. Strictly speaking, Eq. (2-12) holds only for a steady, incompressible flow. However, it is assumed that Eq. (2-12) also approximately holds for a statistically steady flow. Under this assumption, the time-

averaged rate of generation ($\bar{G}$) can be approximated by Reynolds-averaging Eq. (2-12). Reynolds averaging is the process of decomposing an instantaneous quantity (ϕ) into the sum of a time-averaged component ($\bar{\phi}$) and a fluctuating component (ϕ'). The time average of a quantity (denoted by an overbar) is defined as

$$\bar{\phi} = \frac{1}{T}\int_{t_1}^{t_1+T} \phi dt \tag{2-13}$$

where T is the averaging period.

Reynolds-averaging Eq. (2-12) yields

$$\bar{G} = \bar{\tau}_{ij}\frac{\partial \bar{u}_j}{\partial x_i} + \mu\overline{\frac{\partial u_\iota'}{\partial x_\jmath}\frac{\partial u_\iota'}{\partial x_\jmath}} + \mu\overline{\frac{\partial u_\iota'}{\partial x_\jmath}\frac{\partial u_\jmath'}{\partial x_\iota}} \tag{2-14}$$

The first term in Eq. (2-14) is simply the time-averaged viscous dissipation rate. The second term is proportional to the turbulent dissipation rate (ϵ). The third term does not have an obvious physical interpretation. During the course of analysis, it was found to be very small, so it is neglected. Eq. (2-14) can now be written as

$$\bar{G} = \bar{\tau}_{ij}\frac{\partial \bar{u}_j}{\partial x_i} + \rho\epsilon \tag{2-15}$$

By definition, ϵ is

$$\epsilon = \nu\overline{\frac{\partial u_\iota'}{\partial x_\jmath}\frac{\partial u_\iota'}{\partial x_\jmath}} \tag{2-16}$$

While it may not be immediately obvious, $\bar{\tau}_{ij}\frac{\partial \bar{u}_j}{\partial x_i}$ is positive definite. To see this, realize that $\bar{\tau}_{ij}\frac{\partial \bar{u}_j}{\partial x_i}$ can be expressed as

$$\bar{\tau}_{ij}\frac{\partial \bar{u}_j}{\partial x_i} = \frac{1}{2}\mu\left(\frac{\partial \bar{u}_i}{\partial x_j} + \frac{\partial \bar{u}_j}{\partial x_i}\right)^2 \tag{2-17}$$

Since ϵ is also positive definite, the entire right-hand side of Eq. (2-15) is positive definite. This reflects an important physical fact: viscous dissipation and turbulent dissipation *always* act to *increase* profile loss (alternatively, it could be said that viscous dissipation and turbulent dissipation *always* act to *decrease* total pressure).

Often, it is more informative to work with the components of $\bar{G}$ rather than $\bar{G}$ itself. The components of $\bar{G}$ are

$$\bar{G}_{\Phi} = \bar{\tau}_{ij} \frac{\partial \bar{u}_j}{\partial x_i} \tag{2-18}$$

and

$$\bar{G}_{\epsilon} = \rho\epsilon \tag{2-19}$$

$\bar{G}_{\Phi}$ is the loss at a point due only to viscous dissipation. Similarly, $\overline{\mathrm{G}}_{\epsilon}$ is the loss at a point due only to turbulent dissipation. Clearly, $\bar{G} = \bar{G}_{\Phi} + \bar{G}_{\epsilon}$. The total profile loss over an arbitrary region, R, can be found by integrating Eq. (2-15) over R.

Chapter 3: Results

3.1 Low-Re Performance of the L3

3.1.1 Loss and Loading

One metric often used to quantify the performance of an LPT blade is the total pressure loss coefficient:

$$Y = \frac{p_{0,1} - p_{0,2}}{p_{0,1} - p_2} \tag{3-1}$$

In this section, the terms *total pressure loss coefficient* and *loss coefficient* will be used interchangeably as will the terms *total pressure loss* and *loss*. The loss coefficient is plotted as a function of Reynolds number in Fig. 3-1. Reynolds number is defined based on axial chord (C_x) and exit velocity:

$$\mathrm{Re}_\infty = \frac{\rho U_2 C_x}{\mu} \tag{3-2}$$

Note that $p_{0,2}$ was calculated at the exit of the computational domain (a distance of 1 axial chord downstream of the trailing edge; see Fig. 2-1).

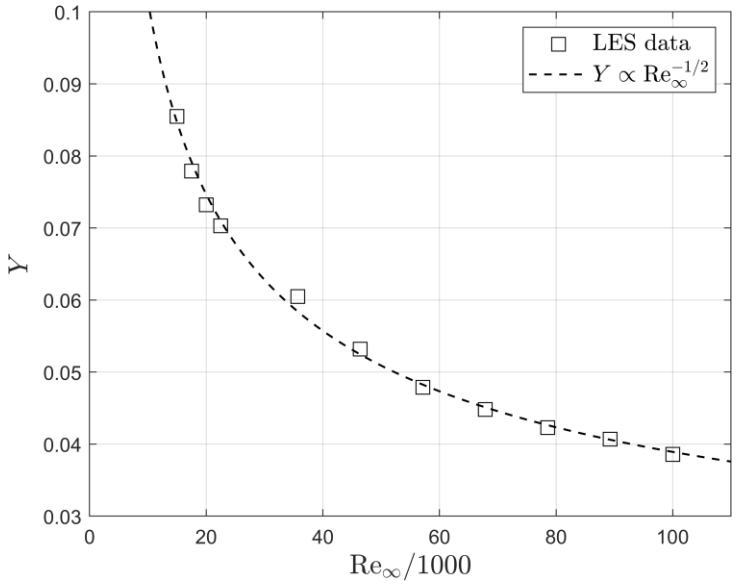

Fig. 3-1: Variation of the total pressure loss coefficient with Reynolds number for the L3FHW-LS.

The loss coefficient increases gradually with decreasing Reynolds number, scaling approximately with $\mathrm{Re}_\infty^{-1/2}$. From this scaling, it can be inferred that viscous dissipation is the dominant source of total pressure loss [68]. At such low Reynolds numbers, one might expect unreattaching boundary layer separation to be the dominant source of loss. As discussed previously, unreattaching boundary layer separation causes loss to increase dramatically—in some cases by as much as 500% [38]. Consequently, unreattaching boundary layer separation is typically apparent as a "knee" (i.e., a point-like discontinuity in the lapse curve across which the loss coefficient increases abruptly) in the lapse curve. There is no indication of such a "knee" in Fig. 3-1, which suggests that unreattaching boundary layer separation does not occur (at least, not over the range of Reynolds number considered). Experiment [45] has confirmed this to be the case.

Time-averaged loading distributions are plotted in Fig. 3-2 for select Reynolds numbers. Like the loss coefficient, the pressure coefficient is referenced to exit conditions:

$$C_p = \frac{p_{0,1} - p}{p_{0,1} - p_2} \tag{3-3}$$

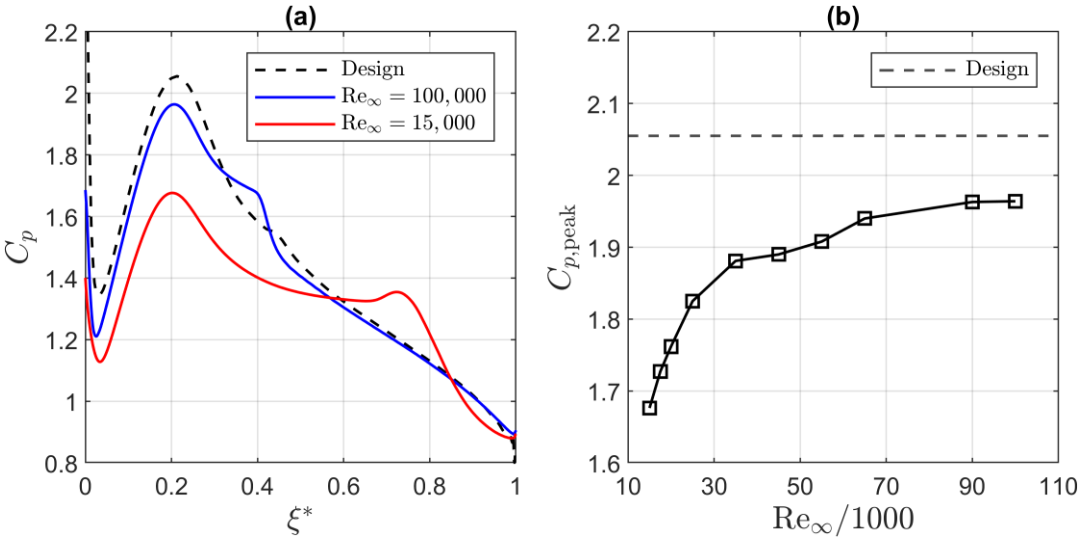

Fig. 3-2: (a) time-averaged loading distributions for the minimum and maximum Reynolds numbers considered in this study (b) variation in peak loading with Reynolds number.

In Fig. 3-2a, ξ^* is the nondimensional length along the suction surface:

$$\xi^* = \xi / L_{\mathrm{ss}} \tag{3-4}$$

At design conditions, C_p increases up unto to the suction peak ($C_{p,\mathrm{peak}}$) then monotonically decreases to the trailing edge. As might be expected, the behavior of the loading profiles differs at off-design conditions. The same general trends are apparent: C_p tends to increase up unto the suction peak then decrease to the trailing edge. However, at off-design conditions, the loading is noticeably lower, and a plateau develops in the pressure coefficient downstream of the suction peak. The decrease in loading and plateau in the pressure coefficient are both strong indications of a separation bubble (in a time-averaged sense).

Judging from the length of the constant pressure plateaus, the separation bubble is ~$0.1L_{\mathrm{ss}}$ in length at $\mathrm{Re}_\infty = 100{,}00$ and to ~$0.6L_{\mathrm{ss}}$ in length at $\mathrm{Re}_\infty = 15{,}000$. Evidently,

the separation bubble grows in length as Reynolds number decreases. As the separation bubble grows in length, its impact on loading becomes more pronounced. At $\mathrm{Re}_\infty = 100{,}000$, the peak pressure coefficient ($C_{p,\mathrm{peak}}$) is only 4% below its design value. By $\mathrm{Re}_\infty = 15{,}000$, $C_{p,\mathrm{peak}}$ has decreased an additional 14%. Peak loading is plotted as a function of Reynolds number in Fig. 3-2b. In general, $C_{p,\mathrm{peak}}$ decreases with decreasing Reynolds number. Interestingly, $C_{p,\mathrm{peak}}$ decreases somewhat abruptly as Reynolds number decreases from ~65,000 to ~35,000. There is definitely a discernable "depression" in the $C_{p,\mathrm{peak}}$ curve over this Range of Reynolds numbers (i.e., the $C_{p,\mathrm{peak}}$ changes concavity over the region).

3.1.2 Boundary Layer Development

Contours of time-averaged streamwise velocity (u_ξ) are plotted in Fig. 3-3 for select Reynolds numbers. They confirm what was already evident from the pressure distributions, namely that a separation bubble is present in a time-averaged sense and grows in length with decreasing Reynolds number.

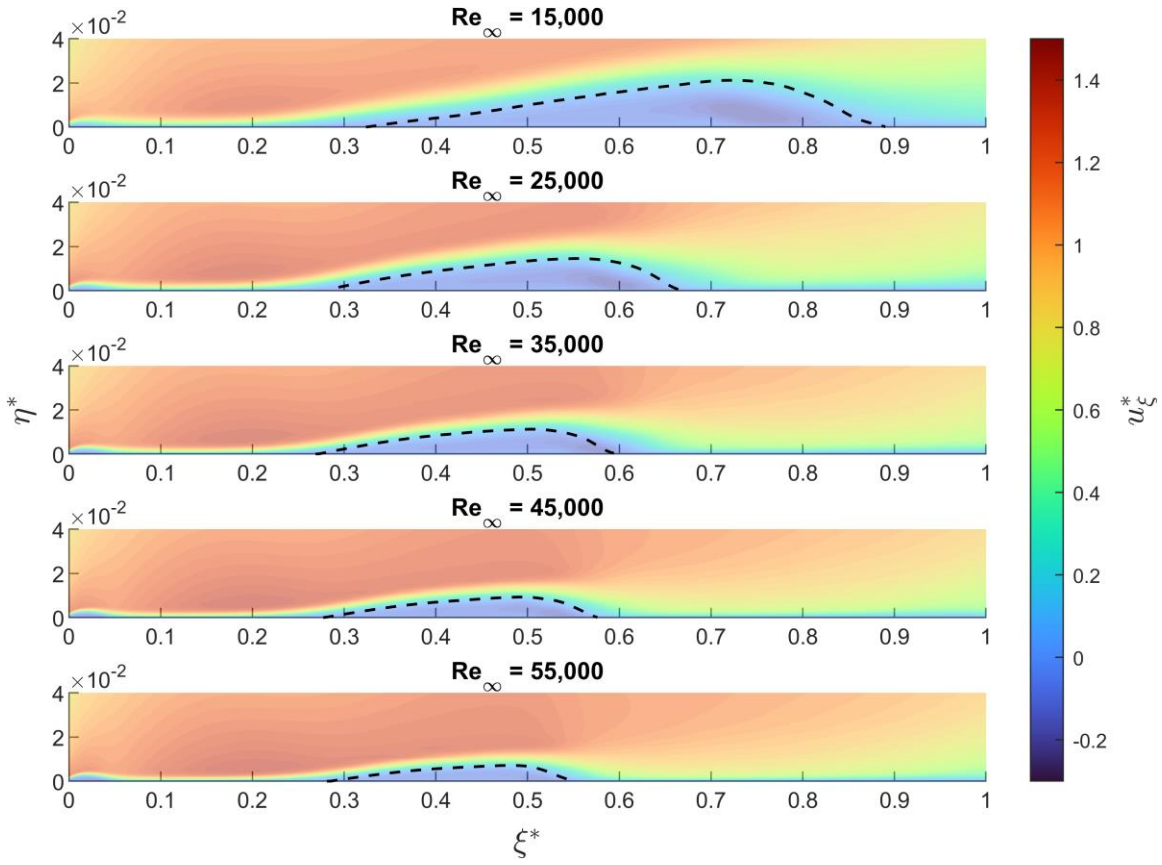

Fig. 3-3: Contours of nondimensional streamwise velocity plotted in $\xi\eta$ space for select Reynolds number. Dashed black line marks mean dividing streamline.

In Fig. 3-3, η^* is the nondimensional wall-normal distance

$$\eta^* = \eta / L_{ss} \tag{3-5}$$

and u_ξ^* is the nondimensional streamwise velocity

$$u_\xi^* = u_\xi / U_2 \tag{3-6}$$

Note that ξ and η form an orthogonal curvilinear coordinate system, as depicted in Fig. 3-4. This coordinate system will frequently be used to help visualize the near wall flowfield.

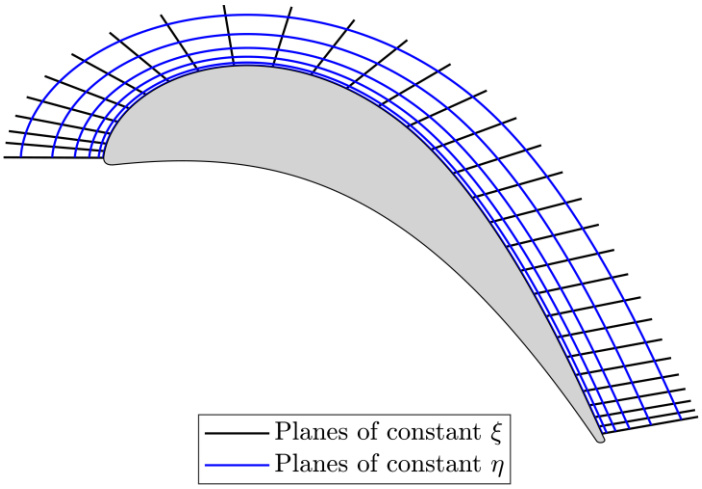

Fig. 3-4: $\xi\eta$ coordinate system plotted in xy space.

In Fig. 3-3, the separation bubble can be identified as the region enclosed by the mean dividing streamline (dashed black line) and the suction surface. The mean dividing streamline constitutes the edge of the separation bubble. That is, it divides the separation bubble from the rest of the flow (hence the name dividing streamline). It is typically regarded as the collection of points across each velocity profile at which the integrated streamwise mass flux is zero. At any streamwise position (ξ_i), the height of the mean dividing streamline (h_d) is given by

$$\int_0^{h_d} \rho u_\xi(\xi_i, \eta) d\eta = 0 \tag{3-7}$$

The mean dividing streamline is used to define the height (h) of the separation bubble:

$$h = \max(h_d) \tag{3-8}$$

The length of the separation bubble (l) is simply the distance between the separation point (ξ_S) and the reattachment point (ξ_R). l and h are depicted schematically in Fig. 3-5.

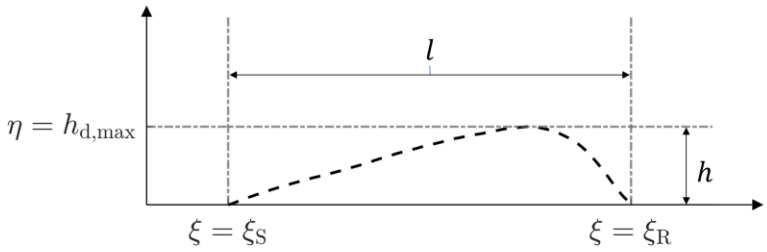

Fig. 3-5: Schematic illustrating how l and h are defined for a separation bubble.

An example skin friction coefficient (C_f) distribution is plotted in Fig. 3-6. In Fig. 3-6a, C_f is plotted as a function of ξ. In Fig. 3-6b, C_f is plotted as a function of the local momentum thickness Reynolds number (Re_θ). This was done to facilitate comparison with the well-known correlation of Schlichting [69]:

$$C_f = 0.0256\mathrm{Re}_\theta^{-0.25} \tag{3-9}$$

Note that Eq. (3-9) is valid only for turbulent flows.

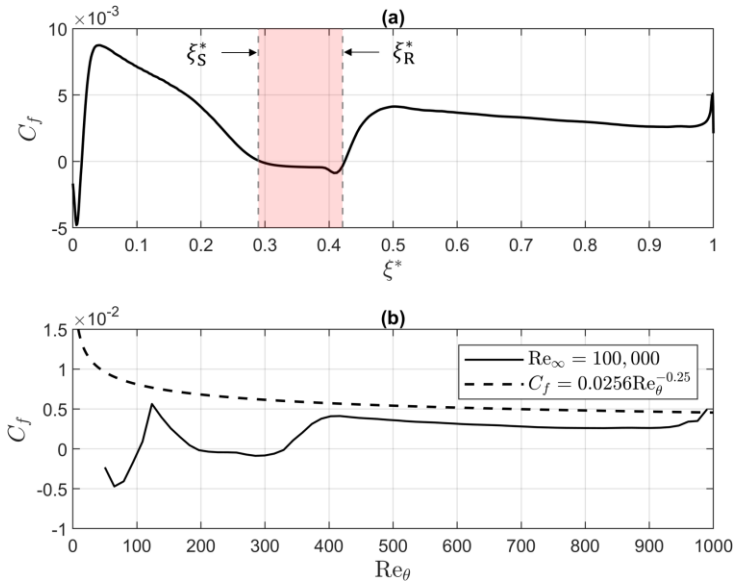

Fig. 3-6: Skin friction coefficient (a) plotted as a function of streamwise distance (b) plotted as a function of Re_θ alongside the correlation of Schlichting [69] for $\mathrm{Re}_\infty = 100{,}000$.

Owing to the strongly favorable pressure gradient upstream of the suction peak, C_f rapidly increases up to a global maximum. As the boundary layer encounters the adverse pressure

gradient on the aft side of the suction surface, C_f decreases and eventually becomes negative when the boundary layer separates. As the separated shear layer reattaches, C_f rapidly increases again before gradually decreasing as the turbulent boundary layer relaxes toward equilibrium. In the turbulent region, downstream of reattachment, the agreement between C_f and the correlation of Schlichting [69] is good, considering the correlation was developed for zero-pressure gradient flow. Since the flow is under an adverse pressure gradient (which acts to reduce C_f), the correlation tends to overpredict C_f. Almost perfect agreement can be obtained if the correlation of Schlichting [69] if shifted by -0.002.

What about the behavior of C_f within the separation bubble? The general behavior of C_f is the same across all Reynolds numbers outside the separation bubble (i.e., $\xi < \xi_S \cup \xi > \xi_R$). However, the same is not true within the separation bubble (i.e., $\xi_S \leq \xi \leq \xi_R$). To illustrate this point, C_f is plotted in Fig. 3-7 for $\xi_S \leq \xi \leq \xi_R$; only select Reynolds numbers are shown.

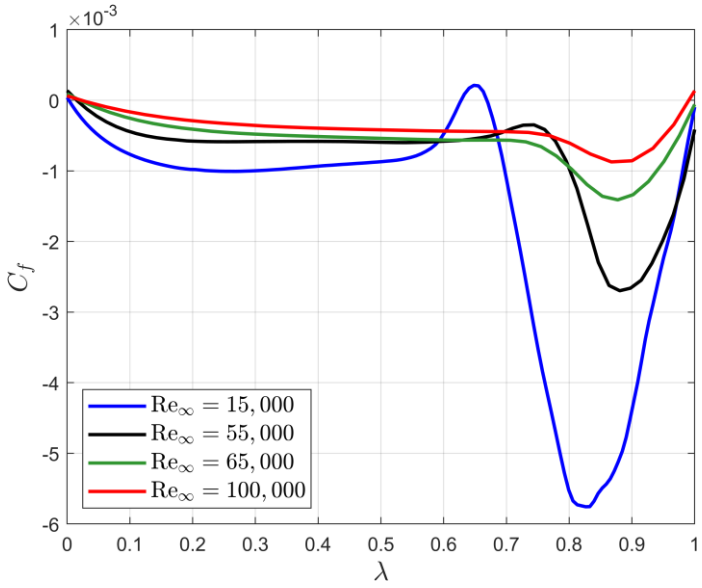

Fig. 3-7: Distribution of the skin friction coefficient within the separation bubble for select Reynolds numbers.

In Fig. 3-7, λ is a measure of the distance along the separation bubble:

$$\lambda = \frac{\xi - \xi_S}{l} \tag{3-10}$$

$\lambda = 0$ corresponds to the separation point and $\lambda = 1$ corresponds to the reattachment point. Within the separation bubble, C_f exhibits two different trends. For $\mathrm{Re}_\infty \geq 65\mathrm{k}$, C_f monotonically decreases to a global minimum ($C_{f,\min}$) then returns to 0 as the flow reattaches. For $\mathrm{Re}_\infty < 65\mathrm{k}$, the behavior of C_f is much the same, except for one notable difference: before decreasing to $C_{f,\min}$, C_f first increases up to a local maximum ($C_{f,\max}$). $C_{f,\max}$ increases as Reynolds number decreases, eventually becoming positive for sufficiently low Reynolds numbers. This is interesting. The near-wall flow (i.e., $\eta \ll h$) is typically reversed everywhere within the separation bubble; in fact, flow reversal is one of the defining characteristics of boundary layer separation. Yet, for certain Reynolds numbers (e.g. $\mathrm{Re}_\infty = 15\mathrm{k}$), $C_{f,\max}$ is positive. What causes the flow to exhibit attached-like behavior (i.e., have a positive value of C_f) and why for only certain Reynolds numbers?

Interestingly, $C_{f,\max}$ occurs at $\lambda \approx 2/3$ (i.e., $2/3$ the way along the separation bubble) for all Reynolds numbers. While λ_{R1} is approximately constant, ξ_{R1} varies considerably with Reynolds number. Here, the subscript *R1* is used to denote the location of $C_{f,\max}$. To illustrate this point, ξ^*_{R1} is tabulated as a function of Reynolds number in Table 3-1.

Table 3-1: Streamwise location of $C_{f,\max}$ tabulated as a function of Reynolds number.

$\mathbf{Re_\infty/1000}$	$\boldsymbol{\xi^*_{R1}}$
15	0.70
20	0.62
25	0.55
35	0.52
45	0.50
55	0.49

ξ_S and ξ_R were calculated from the C_f distributions and are plotted as a function of Reynolds number in Fig. 3-8 and tabulated in Table 3-2.

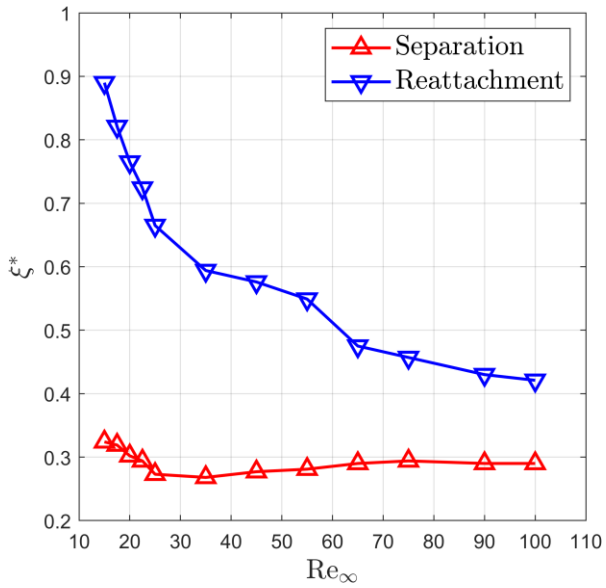

Fig. 3-8: Separation and reattachment point plotted as a function of Reynolds number.

Table 3-2: Separation and reattachment point tabulated as a function of Reynolds number.

$\mathbf{Re_\infty/1000}$	ξ_S^*	ξ_R^*
15	0.32	0.89
20	0.30	0.77
25	0.27	0.67
35	0.27	0.59
45	0.28	0.57
55	0.28	0.55
65	0.29	0.48
75	0.29	0.46
90	0.29	0.43
100	0.29	0.42

To a good first approximation, ξ_S is constant, varying by only a few percent of L_{ss}. That being said, the behavior of ξ_S is noticeable different for very low Reynolds numbers. For $Re_\infty \geq 30{,}000$, ξ_S shifts upstream as Reynolds number is decreased. For $Re_\infty < 30{,}000$, ξ_S shifts downstream as Reynolds number is decreased. The behavior of ξ_S for $Re_\infty < 30{,}000$ is a bit counterintuitive. Why does the separation point shift downstream rather than upstream? As evident in Fig. 3-2, the separation bubble modifies the pressure distribution around the airfoil. For $Re_\infty \leq 30{,}000$, the separation bubble modifies the pressure distribution in such a way as to allow the laminar boundary layer to remain attached slightly longer. ξ_S shifts downstream as a result.

Unlike ξ_S, ξ_R continually shifts downstream as Reynolds number is decreased. For reasons that are not yet clear, ξ_R abruptly shifts downstream as Reynolds number decreases from 65,000 to 55,000. Interestingly, this is the same range of Reynolds numbers over which $C_{p,\text{peak}}$ was observed to decrease abruptly.

The conditions at ξ_S are summarized in Table 3-3 in terms of the shape factor (H), Re_θ, and the Pohlhausen parameter (Po). The Polhausen parameter is defined as

$$\mathrm{Po} = Re_\theta^2 K \tag{3-11}$$

where K is the acceleration parameter:

$$K = \left(\frac{\nu}{U_e}\right)^2 \frac{dU_e}{d\xi} \tag{3-12}$$

Table 3-3: Flow conditions are separation.

$\mathbf{Re_\infty/1000}$	$\boldsymbol{H_S}$	$\mathbf{Re_{\theta,S}}$	$\mathbf{Po_S}$
15	3.9	71	-0.068
20	3.9	78	-0.069
25	3.7	85	-0.077
35	3.6	100	-0.079
45	3.5	114	-0.080
55	3.5	131	-0.080
65	3.5	156	-0.086
75	3.5	169	-0.087
90	3.5	180	-0.087
100	3.5	192	-0.087

At separation, $H \approx 3.5$ and $\mathrm{Po} \approx -0.08$. $\mathrm{Re_\theta}$ increases approximately linearly with $\mathrm{Re_\infty}$. For a laminar boundary layer, $H = 3.5$ at separation [71]. Except for very low Reynolds numbers, $\mathrm{Po_S}$ agrees well with the empirical value of -0.082 suggested by Thwaites [72]. This lends credence to the theory that the separation bubble slightly delays separation for $\mathrm{Re_\infty} < 30{,}000$.

The displacement thickness δ^*, momentum thickness θ, and shape factor H are presented in Fig. 3-9 as a function of ξ^*.

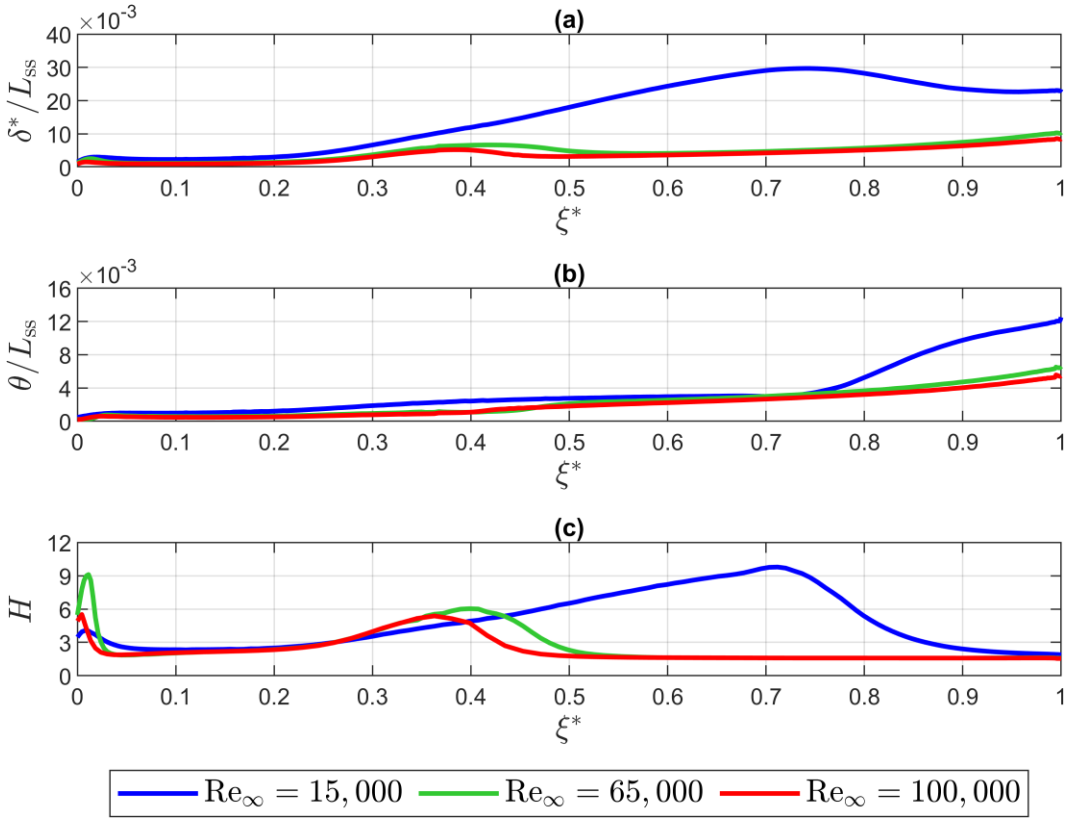

Fig. 3-9: Distribution of the (a) displacement thickness (b) momentum thickness and (c) shape factor along the suction surface of the L3 for select Reynolds numbers.

For all Reynolds numbers, H increases up to a local maximum, then decreases to a value of between $2.4 - 2.5$. This is the expected value for a laminar, accelerated boundary layer [34]; for reference, $H = 2.6$ for a laminar boundary layer under zero pressure gradient. The initial increase in the shape factor is the result of a small LSB that develops near the leading edge. The shape factor remains approximately constant through the end of the favorable pressure gradient region but increases rapidly when the boundary layer separates. Upon separation, the displacement thickness increases sharply, but the momentum thickness remains approximately constant, leading to the observed increase in H. The maximum value of H in this region is associated with the onset of transition [70]. As the boundary layer reattaches, the displacement thickness decreases, and the momentum thickness

increases. H decreases as a result. For $\mathrm{Re}_\infty > 25\mathrm{k}$, $H \approx 1.6$ at the trailing edge. This is consistent with the shape of a turbulent boundary layer and is identical to the shape factor reported by Volino [34] in his study of an LPT airfoil. For $\mathrm{Re}_\infty \leq 25{,}000$, H is larger at the trailing edge, with a value of $\sim$1.9. For reference, $H = 1.4$ for a turbulent boundary under zero pressure gradient.

While the shape factor at the trailing edge is only slightly higher for $\mathrm{Re}_\infty \leq 25\mathrm{k}$, the turbulent boundary layer is significantly less mature. Trailing edge boundary layer profiles are plotted for select Reynolds numbers in Fig. 3-10.

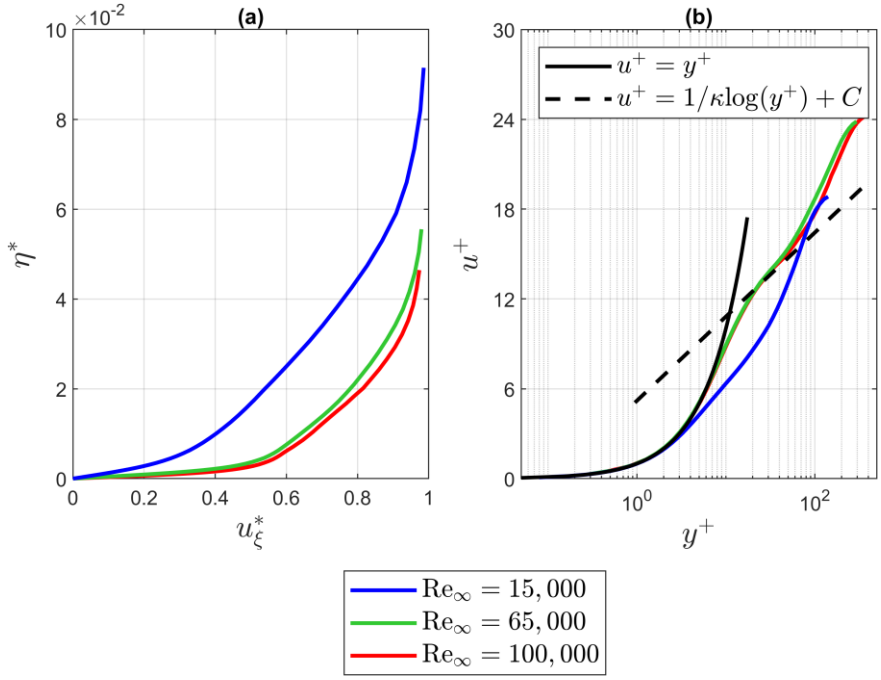

Fig. 3-10: Trailing edge boundary layer profiles plotted (a) as a function of η (b) as a function of y^+.

In Fig. 3-10a, the trailing edge boundary layer profile is plotted for $0 \leq \eta \leq \delta$, where δ is the boundary layer thickness. As expected, the trailing edge boundary layer grows thinner with increasing Reynolds number. This trend is also apparent in Fig. 3-9a and Fig. 3-9b. The boundary layer profile also grows "fuller" as Reynolds number increases. A full

velocity profile is a hallmark of a turbulent boundary layer. As the profile grows fuller, the velocity gradient across the inner region (i.e., the viscous sublayer) steepens.

In Fig. 3-10b the trailing edge boundary layer profile is plotted alongside the "law of the wall" [73]. Consistent with the recommendations of Bradshaw and Huang [73], κ is taken to be 0.41 and C is taken to be 5.2. As can be seen, the turbulent boundary layer is significantly more mature for $\mathrm{Re}_\infty = 65\mathrm{k}$ and $\mathrm{Re}_\infty = 100\mathrm{k}$. For low Reynolds numbers, the reattachment point is very close to the trailing edge, leaving the emergent turbulent boundary layer little room to mature. For example, reattachment occurs only $0.1L_{\mathrm{ss}}$ (equivalently, $\sim 0.2l$) upstream of the trailing edge at $\mathrm{Re}_\infty = 15\mathrm{k}$. According to Alam and Sandham, it may take as many as 7 bubble lengths to recover a typical turbulent profile [74].

3.1.3 Transition

At this point, it is clear that a separation bubble is present in a time average sense. While there have been indications that the flow is laminar at separation (e.g., Table 3-3), this fact has not been conclusively established. To determine whether the separation bubble is laminar, transitional, or turbulent, it is necessary to determine where the flow transitions (i.e., before or after separation).

The transition point was identified using the intermittency algorithm of Volino et al. [60], as discussed previously. Example intermittency contours are plotted in Fig. 3-11 for $\mathrm{Re}_\infty = 15{,}000$.

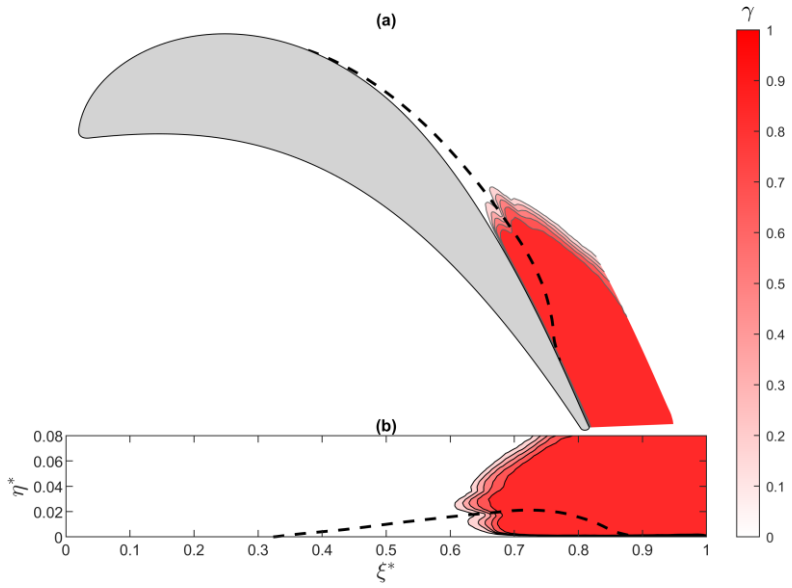

Fig. 3-11: Intermittency contours plotted in (a) xy space and (b) $\xi\eta$ space for $\mathrm{Re}_\infty = 15{,}000$. Dashed black lines marks mean dividing streamline.

The intermittency is 0 at separation. While only one Reynolds number is depicted in Fig. 3-11, separation always precedes transition. For all Reynolds numbers, the boundary layer begins laminar and eventually transitions to turbulence at some point in the adverse pressure gradient region downstream of the separation point. Thus, the separation bubble is indeed laminar.

The transition point, $(\xi_\mathrm{t}, \eta_\mathrm{t})$, was defined as the first point at which the following two conditions were met: 1) $\gamma(\xi, \eta) > 0.01$ and 2) $\eta > h(\xi)$. The second condition ensures the transition point lies in the shear layer, outside of the separation bubble (i.e., outside the region enclosed by the mean dividing streamline and the suction surface). Similarly, the transition end point $(\xi_\mathrm{T}, \eta_\mathrm{T})$ was defined as the first point at which $\gamma(\xi, \eta) > 0.99$ and $\eta > h(\xi)$. Between ξ_t and ξ_T (i.e., in the transition region), γ increases exponentially from 0 to 1, as depicted in Fig. 3-12. Note that the max intermittency at each streamwise location, γ_max, is plotted rather than the intermittency at every point (as in Fig. 3-11).

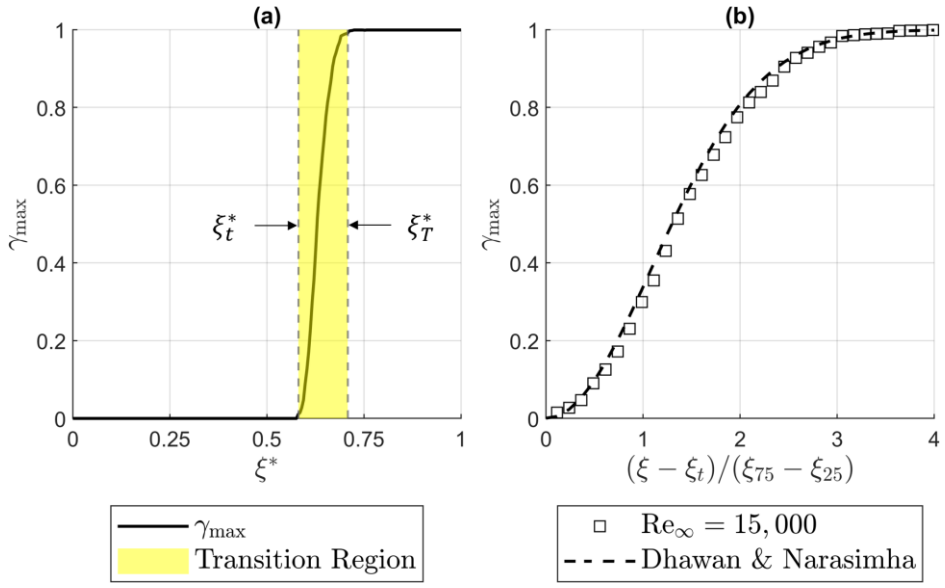

Fig. 3-12: Peak intermittency for $\mathrm{Re}_\infty = 15{,}000$ plotted (a) as a function of streamwise distance (b) alongside the universal intermittency distribution of Dhawan & Narasimha [75].

$\gamma_{\max}$ is 0 up unto $\xi^* \approx 0.6$, at which point it increases rapidly before saturating around $\xi^* = 0.7$. The point at which $\gamma_{\max}$ first begins to increase roughly corresponds to ξ_t^* (the exact location of ξ_t^* is determine by the two conditions discussed previously). Similarly, the point at which $\gamma_{\max}$ saturates roughly corresponds to ξ_T^*. Note that the actual locations of ξ_t^* and ξ_T^* (i.e., not approximate) are plotted in Fig. 3-12a.

In Fig. 3-12b, $\gamma_{\max}$ is plotted alongside the universal intermittency distribution of Dhawan & Narasimha [75]:

$$\gamma = 1 - \exp\left[-0.412\left(\frac{\xi - \xi_t}{\xi_{75} - \xi_{25}}\right)^2\right] \tag{3-13}$$

In Eq. (3-13), ξ_{75} is the location at which $\gamma = 0.75$; similarly, ξ_{25} is the location at which $\gamma = 0.25$. While the universal intermittency distribution was originally developed for zero-pressure-gradient flows, numerous studies (e.g., Volino and Hultgren [76] and Sharma et

al. [77]) have shown it to be valid for a broad range of conditions. The variation of γ in the transition region is well-described by the universal intermittency distribution.

The transition point, separation point, and reattachment point are plotted as a function of Reynolds number in Fig. 3-13a.

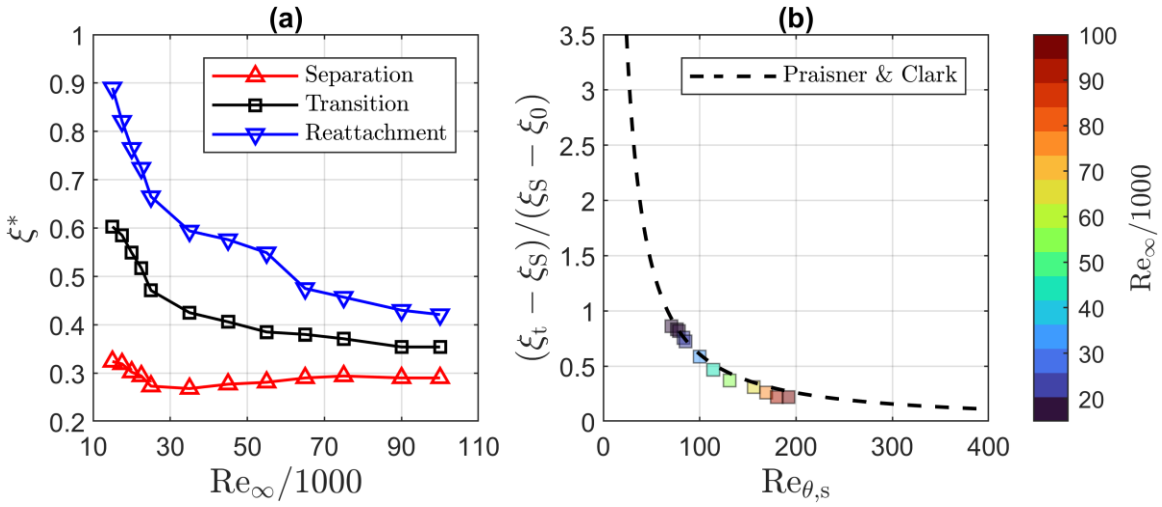

Fig. 3-13: (a) separation, transition, and reattachment points plotted as a function of Re_∞ (b) transition plotted as a function of Re_θ alongside the correlation of Praiser and Clark [38].

Fig. 3-13a makes clear that separation always precedes transition. In general, ξ_t shifts downstream as Reynolds number decreases, much like ξ_R. However, ξ_t does not exhibit the same abrupt change over $55{,}000 \leq \mathrm{Re}_\infty \geq 65{,}000$. The variation of ξ_t with Reynolds number is well described by the correlation of Praiser and Clark [38], as depicted in Fig. 3-13b.

The locations of transition onset (ξ_t) and transition completion (ξ_T) are summarized in Table 3-4.

Table 3-4: Summary of the locations of both transition onset and transition completion. Note that the uncertainty in both ξ_t and ξ_T is $0.01L_{ss}$.

$\mathbf{Re_\infty/1000}$	$\boldsymbol{\xi_t^*}$ $(\pm\mathbf{0.01})$	$\boldsymbol{\xi_T^*}$ $(\pm\mathbf{0.01})$
15	0.60	0.74
20	0.55	0.66
25	0.47	0.55
35	0.43	0.52
45	0.41	0.50
55	0.39	0.48
65	0.38	0.45
75	0.37	0.45
90	0.36	0.43
100	0.35	0.42

For all Reynolds numbers, the uncertainty in the transition point is $0.01L_{ss}$. As discussed earlier, the algorithm of Volino et al. [60] requires the user to choose an appropriate value for C_1. Choosing this threshold is more of an art than a science; ultimately, visual inspection is the best way to determine how well the intermittency function is separating turbulent from non-turbulent samples [63]. Given the uncertainty inherent in choosing C_1, an attempt was made to quantify how this uncertainty affects ξ_t. For each Reynolds number, ξ_t was calculated for 10 different values of C_1 and the max of the standard deviation of ξ_t was taken as the uncertainty. Note: error bars are not drawn in Fig. 3-13 as the uncertainty is so small as not to be discernible at the scale shown.

3.1.4 Evolution of the LSB

The length and height of the LSB are plotted as a function of Reynolds number in Fig. 3-14a and Fig. 3-14b respectively.

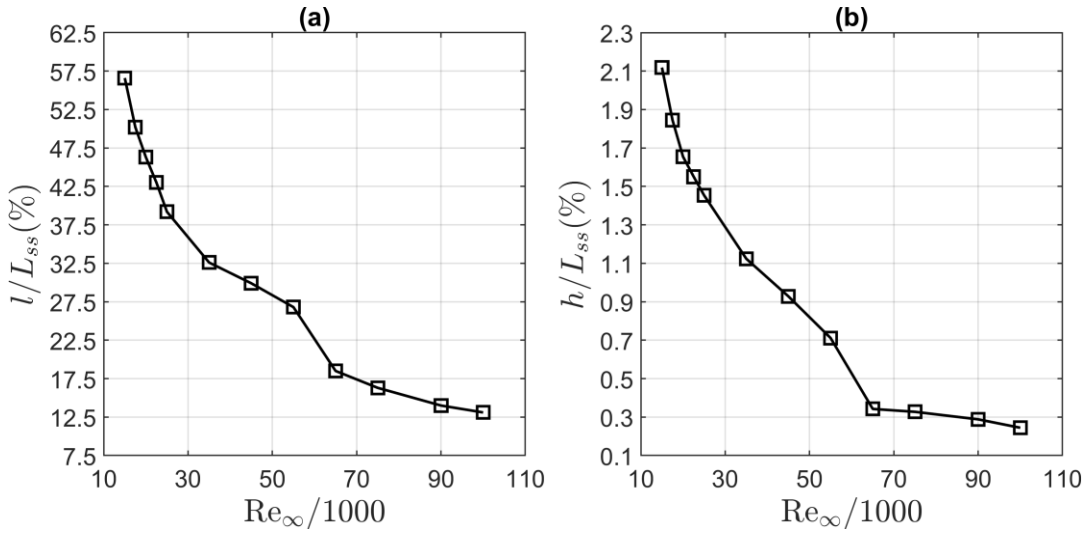

Fig. 3-14: (a) length of the LSB plotted as a function of Reynolds number (b) height of the LSB plotted as a function of Reynolds number.

Interestingly, both l and h increase abruptly as Reynolds number decreases from 65,000 to 55,000; l increases by nearly 60% and h increases by nearly 100%. This is the same range of Reynolds numbers over which ξ_{R} suddenly shifts downstream and the $C_{p,\mathrm{peak}}$ curve changed concavity. All of this is very strong evidence to suggest that the LSB transitions from short to long (i.e., bursts) over this range of Reynolds numbers. Note: $55{,}000 \leq \mathrm{Re}_\infty \leq 65{,}000$ is also the range of Reynolds numbers over which the time-averaged behavior of C_f changed within the separation bubble (see Fig. 3-7); however, at this point it is not clear how this relates to bursting.

The topic of transition is now briefly revisited. For long LSBs ($\mathrm{Re}_\infty > 65{,}000$), transition completion precedes reattachment whereas for short LSBs ($\mathrm{Re}_\infty < 55{,}000$) transition completion is approximately coincident with reattachment. To make this point clear, the distance between transition completion and reattachment ($\xi_{\mathrm{R}}^* - \xi_{\mathrm{T}}^*$) is plotted as a function of Reynolds number in Fig. 3-15.

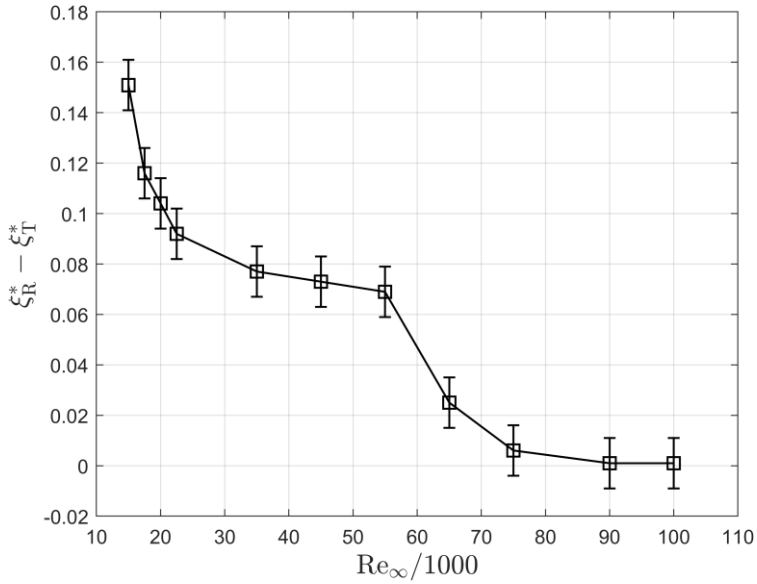

Fig. 3-15: Distance between transition completion and reattachment plotted as a function of Reynolds number.

For $\mathrm{Re}_\infty > 65{,}000$, the final coalescence into turbulence occurs in the vicinity of reattachment. However, for $\mathrm{Re}_\infty < 65{,}000$, the final coalesce into turbulence occurs as much as $\sim 0.2 L_{ss}$ upstream of reattachment. Apparently, significantly more mixing is necessary to bring about reattachment for long LSBs.

It is interesting to note that the reattachment point abruptly shifts downstream when the LSB bursts, but the transition point does not (see Fig. 3-13). This lends credence to the theory that bursting is independent of the transition process and occurs as a result of a sudden failure of the shear layer to reattach [27,29]. Hatman and Wang [27] go so far as to claim that short and long LSBs are "identical" up unto transition.

In light of the above discussion, it is now possible to assess the performance of the machine learning model (see Fig. 2-6). The model predicts that bursting occurs over the range $40{,}000 < \mathrm{Re}_\infty < 60{,}000$. This agrees well with the actual range over which bursting occurs, although the lower bound is a bit conservative.

As mentioned earlier, there exist a number of bursting criteria, the most famous of which being due to Gaster [31]. Data from the present study is plotted on top of the bursting diagram of Gaster in Fig. 3-16.

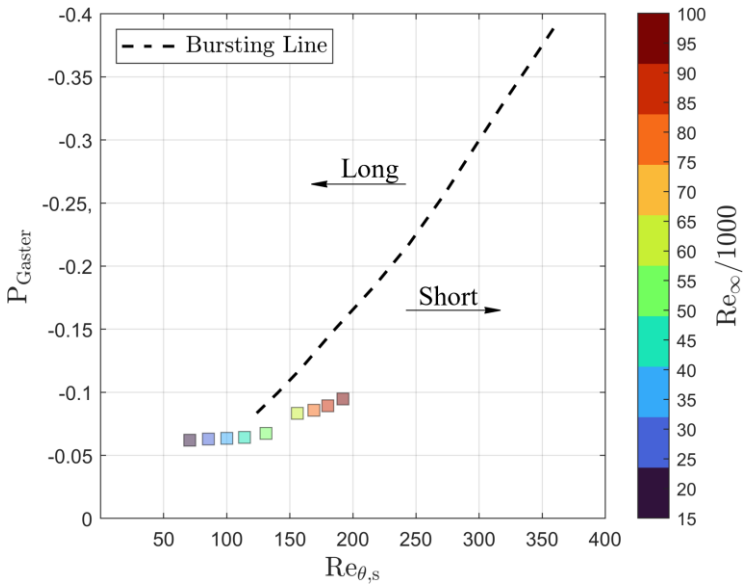

Fig. 3-16: Data from present study plotted on top of the bursting diagram of Gaster [31].

While P_{Gaster} increases rapidly as Reynolds number decreases from 65,000 to 55,000 (i.e., at bursting), the bursting line does not intersect the data over this range. In fact, the bursting line does not intersect the data at all. However, if the bursting line were extrapolated, it would intersect the data around $\text{Re}_\infty = 25{,}000$—significantly below the actual bursting Reynolds number. The bursting criteria of both Diwan et al. [33] and Hatman and Wang [27] were also tested; however, both predicted the LSB is short over the entire Range of Reynolds numbers.

In this study, bursting was caused by a change in Reynolds number rather than a change in incidence. Most bursting criteria (include the criteria of Diwan et al. [33] and Hatman and Wang [27]) were developed for applications in which bursting is caused by a change in incidence. The failure of existing criteria to correctly predict bursting in the

present study suggests that the effects of bursting are more pronounced in applications where bursting is caused by a change in incidence. This is best illustrated by the bursting criterion of Diwan et al. [33]. According to their model, bursting occurs when $P_{\mathrm{Diwan}} < -28$. In this study, the lowest value of P_{Diwan} (occurring at $\mathrm{Re}_{\infty} = 15{,}000$) was approximately -9. Since P_{Diwan} is based on h, this suggests that the change in h is significantly more pronounced if bursting is caused by a change in incidence.

All bursting criteria attempt to answer one question: when does bursting occur? The best answer to this question is probably "you will know it when you see it," which is why the approach of Tani [30] is so popular. There are many things in fluid dynamics that fall under the category of "you will know it when you see it," turbulence being perhaps the best example thereof. This work represents an attempt to quantify the "you-will-know-it-when-you-see-it" approach of Tani using modern (i.e., data-driven) methods.

Relative to existing bursting criteria, the present model shows its utility in two ways. First, it requires only a few pressure measurements. Pressure is easy to measure, especially relative to quantities such as θ or h. Second, the present model is probabilistic rather than deterministic. As Gaster [31] himself acknowledged, bursting is not an instantaneous phenomenon; it occurs over a finite range of Reynolds numbers (or angles of attack). During bursting, an LSB is neither short, nor long; it exists in a sort of "gray" area between the two states. All currently existing models are deterministic. They recognize only two states: short and long. The present model recognizes a continuum of states. Instead of being either short or long, it allows an LSB to be 60% short and 40% long or 90% short and 10% long. In this manner, the present model is more consistent with reality, as bursting is a continuous phenomenon. While the present model performed well

in this work, it likely needs significantly more training data—from a diversity of applications—to perform well in general. With that said, it certainly shows promise.

3.1.5 Section Summary

In this section, the low-Re performance of the L3 was analyzed. Reynolds lapse was found to be relatively benign; remarkably, there was no indication of unreattaching boundary layer separation over the entire range of Reynolds numbers considered. While the suction surface boundary layer did not fully separate, an LSB developed over the aft part of the suction surface and grew longer with decreasing Reynolds number. It was conclusively shown that bursting occurred over the range $55{,}000 \leq \mathrm{Re}_\infty \leq 65{,}000$. The cluster-based bursting criterion developed earlier was found to predict the onset of bursting reasonably well, especially compared to existing bursting criteria.

Upon bursting, h and l increased rapidly. The length of the separation bubble increased not because the separation point changed but because the reattachment point changed. Upon bursting, the reattachment point abruptly shifted downstream. The separation point remained approximately constant through bursting. Bursting was found to have no effect on the location of transition onset, which supports the theory that bursting is independent of the transition process and occurs as a result of a sudden failure of the shear layer to reattach [27,29]. For long LSBs, transition completion occurred upstream (in some cases, as much as $\sim 0.2 L_{\mathrm{ss}}$) of the location of time-averaged reattachment. For short LSBs, transition completion was approximately coincident with the location of time-averaged reattachment.

3.2 Vortex Dynamics

In this section, the dynamics of the vortex shedding process are examined. In a low-disturbance environment, the Kelvin-Helmholtz instability (KHI) is the dominant transition mechanism in a separated shear layer [78]. KHI leads to a roll-up of the vorticity contained in the shear layer into discrete, spanwise vortex structures aptly called "roll-up" vortices [37,78]. These vortices advect downstream where they are eventually shed in a periodic fashion. The goal of this section is to determine what effect—if any—bursting has on the vortex shedding process.

The analysis domain D

$$D = \{(\xi^*, \eta^*) | \, \xi^*_{\mathrm{LE}} \leq \xi^* \leq \xi^*_{\mathrm{TE}}, 0 \leq \eta^* \leq \eta^*_{\max}\} \tag{3-14}$$

is depicted in Fig. 3-17.

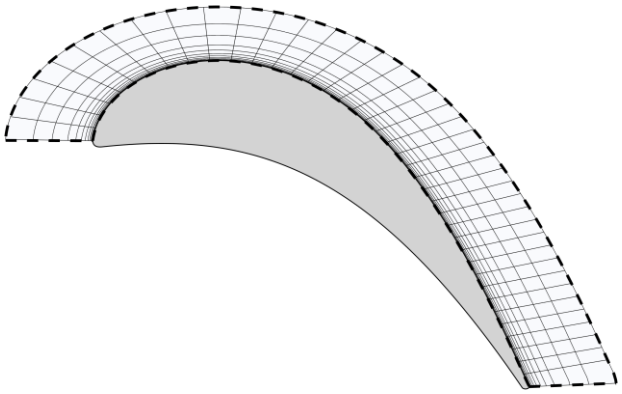

Fig. 3-17: Analysis domain plotted in xy space; every 7th cell is shown in the ξ-direction and every 4th cell is shown in the η-direction.

D includes only the suction surface and its immediate surroundings. The wall-normal extent of D (i.e., $\eta^*_{\max}$) is much greater than the average boundary layer thickness but much less than the pitch. D was discretized into 75 cells in the ξ-direction and 125 cells in the η-direction.

Vortex cores were tracked across both space (i.e., within D) and time using the algorithm of Jiang et al. [64] (with some modifications; see §2.3.2). Two-dimensional histograms of time-averaged core vorticity ($\overline{\omega}_c$) are plotted in Fig. 3-18a and Fig. 3-19a for $\mathrm{Re}_\infty = 15{,}000$ and $\mathrm{Re}_\infty = 25{,}000$, respectively. The same number of bins were used for both Reynolds numbers. ω_c is a piecewise function; at any point, $\omega_c = \omega_z$ if a vortex core exists at that point and 0 otherwise. Two-dimensional histograms of vortex core residence time (t_r) are plotted in Fig. 3-18b and Fig. 3-19b for $\mathrm{Re}_\infty = 15{,}000$ and $\mathrm{Re}_\infty = 25{,}000$, respectively. Again, the same number of bins were used for both Reynolds numbers. As the name suggests, t_r measures the fraction of time a vortex core resides within a given region (e.g., a histogram bin).

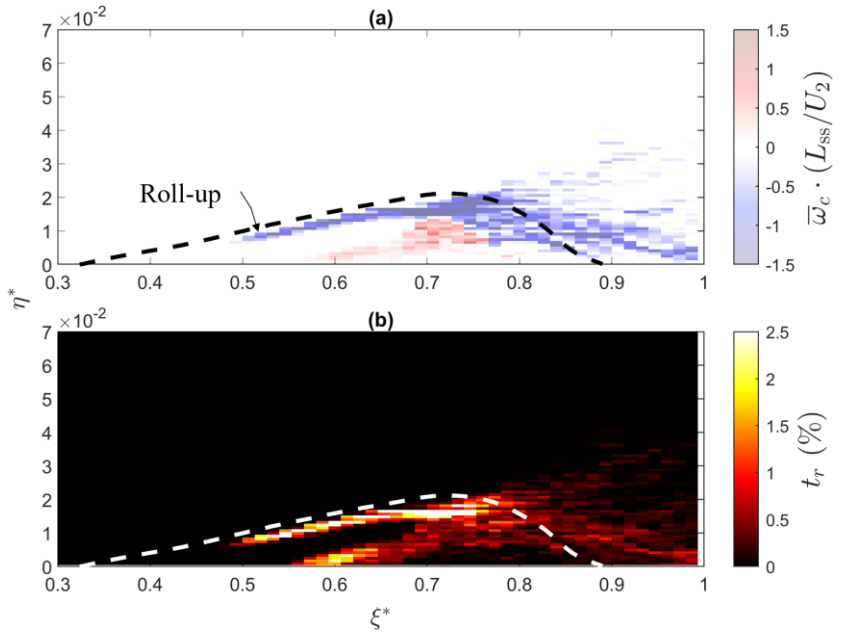

Fig. 3-18: (a) two-dimensional histogram of time-averaged core vorticity; dashed black line marks mean dividing streamline (b) two-dimensional histogram of vortex core residence time; dashed white line marks mean dividing streamline. $\mathrm{Re}_\infty = 15{,}000$ shown.

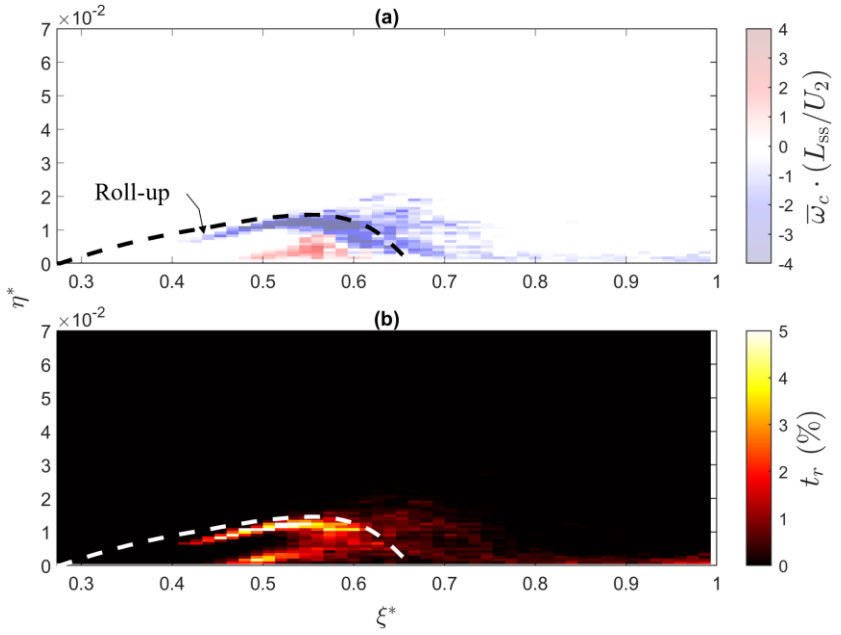

Fig. 3-19: (a) two-dimensional histogram of time-averaged core vorticity; dashed black line marks mean dividing streamline (b) two-dimensional histogram of vortex core residence time; dashed white line marks mean dividing streamline. $\mathrm{Re}_\infty = 25{,}000$ shown.

For $\mathrm{Re}_\infty = 15{,}000$, the roll-up vortex forms around $\xi^* = 0.5$. It then advects downstream before being shed around $\xi^* = 0.75$; this location approximately corresponds to the location of $h_{d,\max}$. Before shedding ($0.5 < \xi^* < 7.5$), the roll-up vortex follows a clearly defined path that is closely aligned with the mean dividing streamline. After shedding ($\xi^* > 0.75$), the roll-up vortex no longer follows a clearly defined path; however, on average, it still follows the mean dividing streamline—at least, up unto the location of time-averaged reattachment. The same trends described above for $\mathrm{Re}_\infty = 15{,}000$ are also apparent for $\mathrm{Re}_\infty = 25{,}000$.

Interestingly, a second vortex appears to develop around $\xi^* = 0.6$ for $\mathrm{Re}_\infty = 15{,}000$. Its rotation is opposite that of the roll-up vortex, as $\overline{\omega}_c$ is positive rather than negative. For reasons that will become clear later, this vortex will be referred to as the *induced* vortex. The induced vortex develops very near the suction surface ($\eta^* < 0.01$). It

is relatively weak when it develops but quickly grows in strength as it migrates away from the suction surface. From Fig. 3-19 alone, it is not clear if the induced vortex merges with the roll-up vortex or is ejected into the freestream. Again, the same trends described above for $\mathrm{Re}_\infty = 15{,}000$ are also apparent for $\mathrm{Re}_\infty = 25{,}000$. At this point, two questions come to mind: what causes the induced vortex and is it present for all Reynolds numbers? These questions will be answered in turn.

The induced vortex is produced by a process that will be referred to as *vortex pairing*. In the literature, the term *vortex pairing* is used to refer to two different phenomena. Some authors (e.g., [79]) use the term *vortex pairing* to refer to the process whereby two neighboring vortices merge to form a single, larger vortex. Others (e.g., [80]), use the term to refer to the process whereby two neighboring vortices interact to produce a third vortex of opposite sign. In this research, the term *vortex pairing* is used to refer to the latter phenomenon. This is why the name *induced vortex* was used earlier. The vortex pairing process is depicted in Fig. 3-20 for $\mathrm{Re}_\infty = 15{,}000$.

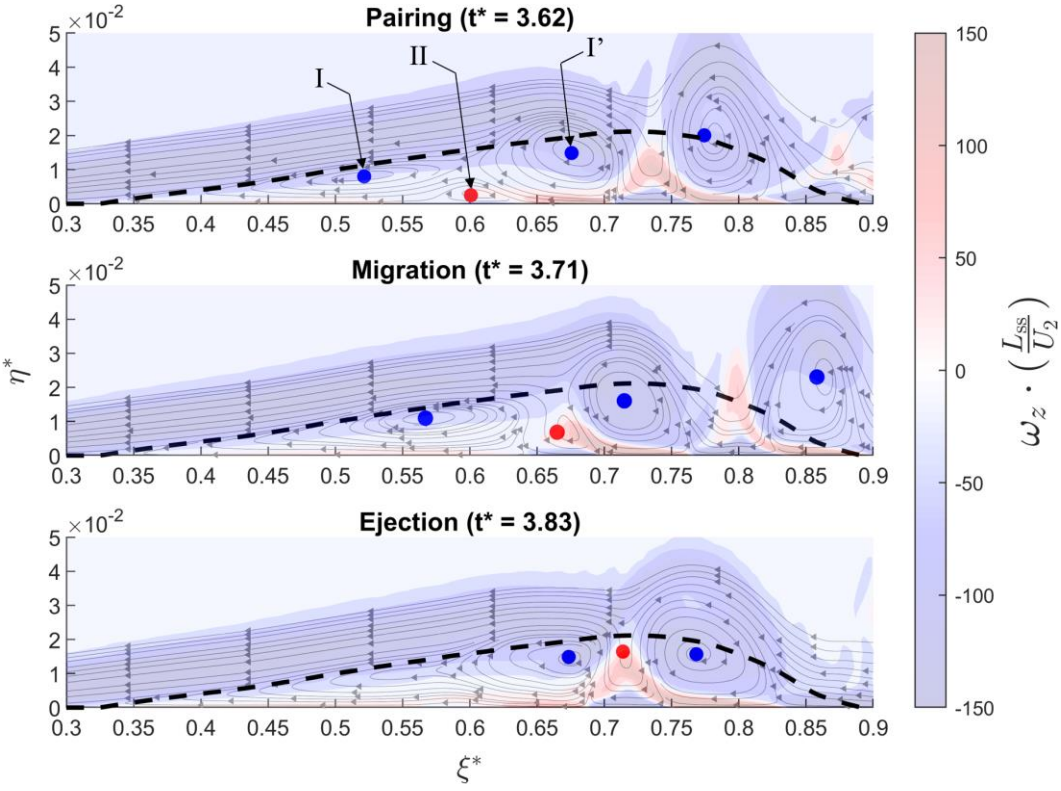

Fig. 3-20: Time series depicting vortex pairing process for $\mathrm{Re}_\infty = 15{,}000$. Each snapshot depicts contours of instantaneous spanwise vorticity overlaid with instantaneous streamlines. Dashed black line marks mean dividing streamline. Positive vortex cores are marked with red circles; similarly, negative vortex cores are marked with blue circles. Vortex core locations were determined using the algorithm of Jiang et al. [64].

The actual pairing process is depicted in the first snapshot of Fig. 3-20. Vortex I and vortex I' are roll-up vortices at varying stages of development. Vortex II is the induced vortex (i.e., the vortex produced by vortex pairing). Vortex II develops in the braid region (i.e., high-shear region) between vortices I and I'. In the first snapshot, vortex II is very near the suction surface. At this stage, it is relatively weak. As time passes, vortex II migrates away from the wall, gaining strength as it does so. Eventually, it is ejected into the shear layer. In examining Fig. 3-18 and Fig. 3-19 earlier, it was unclear if the induced vortex merged with the roll-up vortex or was ejected into the shear later. Fig. 3-20 makes clear that the latter occurs. Previous ejection events can be seen in the first snapshot in Fig. 3-20.

The vortex pairing process alters the time-averaged topology of the LSB, as illustrated by Fig. 3-21

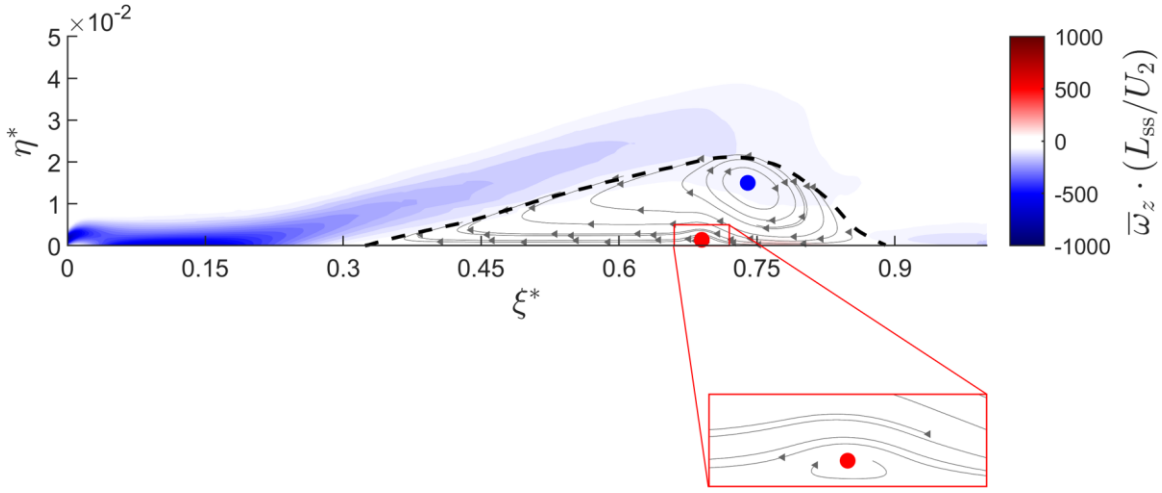

Fig. 3-21: Time-averaged contours of spanwise vorticity overlaid with time-averaged streamlines for $\mathrm{Re}_\infty = 15{,}000$. Induced vortex enlarged for easy viewing. Positive vortex cores are marked with red circles; similarly, negative vortex cores are marked with blue circles. Vortex core locations were determined using the algorithm of Jiang et al. [64].

In a time-averaged sense, there are two vortices present. The negative vortex is the familiar reverse-flow vortex. The positive vortex is not so familiar. Indeed, it marks a departure from the typical time-averaged topology of an LSB [29]. Apparently, this additional vortex arises as a result of the vortex pairing process. Its rotation is opposite that of the reverse-flow vortex. Consequently, it will be referred to as the *counter-rotating vortex*. It is located very near the suction surface, at a streamwise location of approximately $\xi^* = 0.7$.

At this point, an earlier topic is revisited: the time-averaged behavior of C_f in the separation bubble. It was noted earlier that bursting affects the behavior of C_f in the separation bubble, but it was not immediately clear why. Recall, for short LSBs, C_f monotonically decreases to $C_{f,\min}$ then returns to 0 as the flow reattaches. For long LSBs, the behavior of C_f is much the same, except for one notable difference: before decreasing to $C_{f,\min}$, C_f first increases up to $C_{f,\max}$. What causes this behavior? The answer lies in Fig.

3-21. Looking back at Fig. 3-7 and Table 3-1, $C_{f,\max}$ occurs at $\xi^* = 0.7$ for $\mathrm{Re}_\infty = 15{,}000$. This location should sound familiar. It is the location of the counter-rotating vortex. The counter-rotating vortex creates a pocket of flow near the suction surface that is nearly stagnant—at least, relative to the strongly reversed surrounding flow. This pocket of flow shows up as an increase in C_f. Since the counter-rotating vortex arises as a result of vortex pairing, this suggests a correlation between vortex pairing and long LSBs.

To determine if such a correlation exists, the number of pairing events is plotted as a function of Reynolds number in Fig. 3-22. The number of pairing events was estimated by looping over all time steps and counting the number of positive cores that were identified in the region $\xi_S < \xi < \xi_R$. This is a somewhat crude way of estimating the number of pairing events; a far better—and more modern—approach would be to train a machine learning model to recognize pairing events. Machine learning methods excel at pattern-recognition tasks. Since vortex pairing produces a distinctive pattern (see Fig. 3-20), it would likely be trivial to train a machine learning model to identify pairing events. However, this is beyond the scope of the current work.

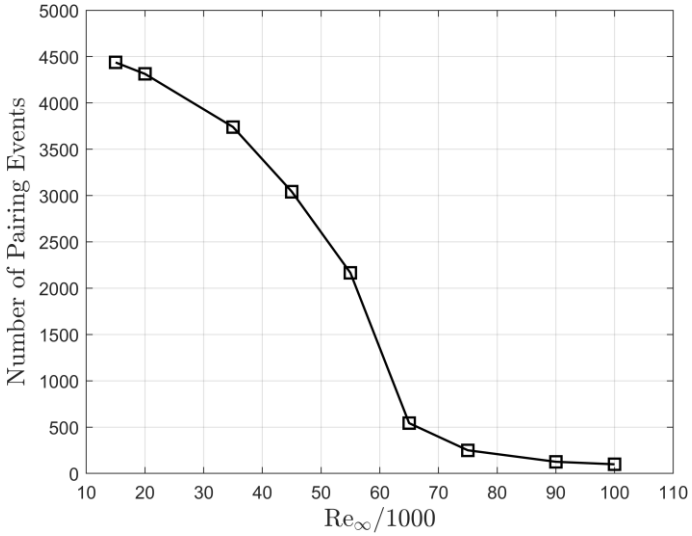

Fig. 3-22: Number of vortex pairing events at each Reynolds number.

Vortex pairing occurs almost exclusively for $\mathrm{Re}_\infty < 65{,}000$; clearly, there is a strong correlation between long LSBs and vortex pairing; At bursting, the number of pairing events increases by over 400%. In reality, this figure is likely much higher. Most of the "pairing events" detected at higher Reynolds numbers are not truly pairing events. Rather, they are simply positive vortex cores that result from the breakdown of the roll-up vortex. At low Reynolds numbers, the roll-up vortex remains coherent past the time-averaged point of reattachment; the same is not true at high Reynolds numbers. As mentioned previously, the present method of detecting pairing events is somewhat crude. However, for its intended purpose, it is more than adequate.

In examining Fig. 3-22, it appears the counter-rotating vortex pushes the reverse-flow vortex up and away from the suction surface. This might indicate that the onset of vortex pairing is what causes h to increase abruptly at bursting. After all, there is a correlation between the onset of vortex pairing and bursting. However, correlation does not necessarily imply causation. It is equally possible that another mechanism causes h to increase at bursting. In this scenario, vortex pairing occurs *because* h increases and not the other way around. Unfortunately, there is insufficient evidence to conclude whether vortex pairing occurs because h increases or h increases because vortex pairing occurs.

3.2.1 Section Summary

In this section it was found that, for short LSBs, vortex shedding proceeded in the usual manner. For long LSBs, vortex pairing was observed to occur. Vortex pairing is the process whereby two neighboring spanwise vortices interact to produce a third vortex of opposite sign. Vortex pairing caused small, counter-rotating vortices to be periodically

ejected into the shear layer. This process altered the time-averaged topology of the LSB to include a second, counter-rotating vortex located beneath the reverse-flow vortex. Since the counter-rotating vortex produced by vortex pairing displaced the reversed-flow vortex, it is possible that the onset of vortex pairing is what drives the rapid increase in h observed at bursting. However, further study is needed to ascertain this.

3.2.2 Loss Analysis

In this section, the profile loss of the L3 is analyzed using the method outlined earlier (see §2.3.3). Throughout this section, the terms *profile loss* and *loss* will be used interchangeably. While profiles loss traditionally includes both the loss generated in the boundary layer of the LPT blade as well as trailing edge loss, the latter is not considered in this analysis. As discussed by Denton [65], trailing edge loss is a function of the momentum thickness at the trailing edge (θ_{TE}) and the geometry of the blade. Since θ_{TE} is known (see Fig. 3-9), the trailing edge loss can be approximated using any of the relations available in the literature (e.g., the relation of Denton [65]). The goal of this section is to determine how bursting affects loss.

The analysis domain D is the same as that used in the previous analysis (see Eq. (3-14) and Fig. 3-17). Since the suction surface boundary layer is the primary source of profile loss [67], D need only include the suction surface and its immediate surroundings. For the present analysis, D was discretized into 320 cells in the ξ-direction and 50 cells in the η-direction—significantly more than in the previous analysis.

It is necessary to introduce two new quantities: the two-dimensional viscous loss distribution function $\bar{\zeta}_{\Phi}(\xi,\eta)$ and the two-dimensional mixing loss distribution function

$\bar{\zeta}_\epsilon(\xi,\eta)$. The former describes how losses due to viscous dissipation are distributed over D and the latter describes how losses due to trubulent dissipation are distributed over D. Both functions are defined only at cell centers. Given a cell with center (ξ_{ij},η_{ij}) and volume ΔV

$$\bar{\zeta}_\Phi(\xi_{ij},\eta_{ij}) = \int_{\Delta V} \bar{G}_\Phi \mathrm{d}V \tag{3-15}$$

and

$$\bar{\zeta}_\epsilon(\xi_{ij},\eta_{ij}) = \int_{\Delta V} \bar{G}_\epsilon \mathrm{d}V \tag{3-16}$$

All integrals were evaluated using a 1-point Gaussian quadrature. For example,

$$\int_{\Delta V} \bar{G}_\Phi \mathrm{d}V \approx \bar{G}_\Phi(\xi_{ij},\eta_{ij})\Delta V \tag{3-17}$$

$\bar{G}_\Phi(\xi_{ij},\eta_{ij})$ and $\bar{G}_\epsilon(\xi_{ij},\eta_{ij})$ were found by taking the cell-wise averages of $\bar{G}_\Phi$ and $\bar{G}_\epsilon$, respectively. The process of computing $\bar{\zeta}_\Phi(\xi,\eta)$ and $\bar{\zeta}_\epsilon(\xi,\eta)$ for a single cell is depicted schematically in Fig. 3-23.

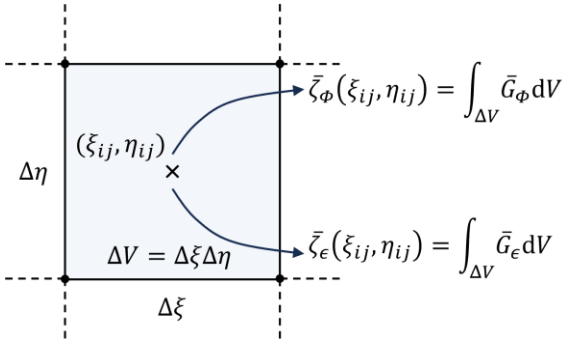

Fig. 3-23: Depiction of the process for computing $\bar{\zeta}_\Phi(\xi,\eta)$ and $\bar{\zeta}_\epsilon(\xi,\eta)$ for a single cell

The two-dimensional distribution functions form a sort of 'basis' for describing loss. As will be seen, many quantities can be expressed in terms of these functions.

Contours of $\bar{\zeta}_{\Phi}(\xi,\eta)$ and $\bar{\zeta}_{\epsilon}(\xi,\eta)$ are plotted in Fig. 3-24 and Fig. 3-25 for $\mathrm{Re}_{\infty} = 15{,}000$ and $\mathrm{Re}_{\infty} = 25{,}000$, respectively. In both figures, the loss distribution functions are nondimensionalized by the total loss ($\bar{Z}$) over D:

$$\bar{Z} = \int_{0}^{\eta_{\max}} \int_{\xi_{\mathrm{LE}}}^{\xi_{\mathrm{TE}}} [\bar{\zeta}_{\Phi}(\xi,\eta) + \bar{\zeta}_{\epsilon}(\xi,\eta)] d\xi d\eta \tag{3-18}$$

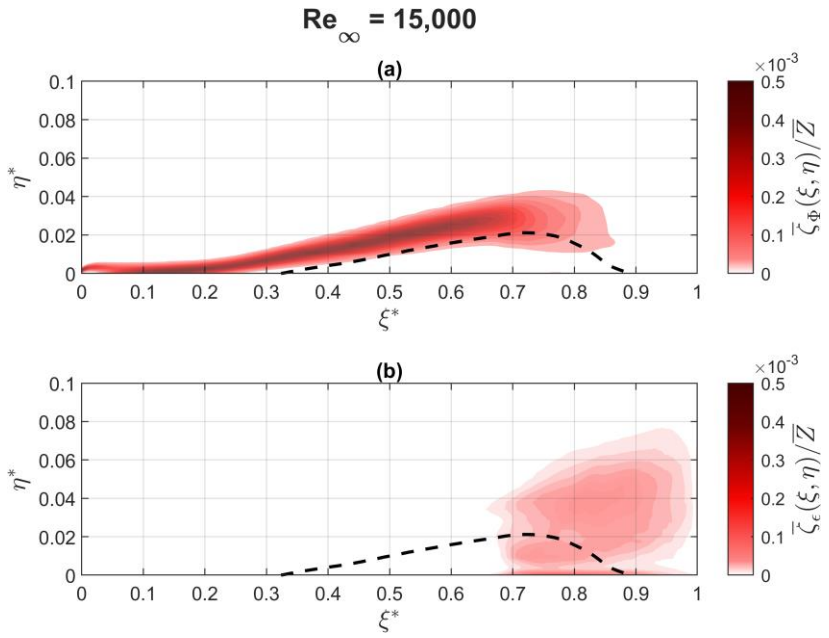

Fig. 3-24: (a) contours of two-dimensional viscous loss distribution function (b) contours of two-dimensional mixing loss distribution function. Dashed black line marks mean dividing streamline.

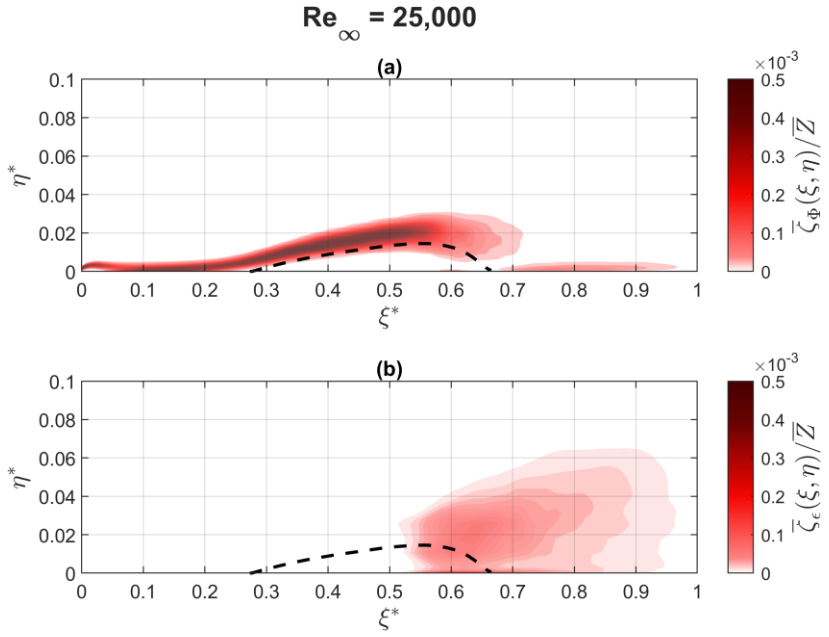

Fig. 3-25: (a) contours of two-dimensional viscous loss distribution function (b) contours of two-dimensional mixing loss distribution function. Dashed black line marks mean dividing streamline.

Prior to transition completion, the dominant source of loss is viscous dissipation in the shear layer. After transition completion, mixing also contributes to loss; however, it is not clear what the dominant loss generation mechanism is in this region. Mixing losses are highest near $h_{d,\max}$. Recall, $h_{d,\max}$ is the maximum displacement of the mean dividing streamline. The elevated mixing loss near $h_{d,\max}$ is a result of the ejection-shedding process. For long LSBs, vortex pairing also likely contributes to loss in this region.

To better understand the development of profile loss along the suction surface, η is integrated out of the two-dimensional loss distributions to yield one-dimensional loss distributions. The one-dimensional viscous loss distribution

$$\bar{\zeta}_\Phi(\xi) = \int_0^{\eta_{\max}} \bar{\zeta}_\Phi(\xi,\eta)\,\mathrm{d}\eta \tag{3-19}$$

describes how losses due to viscous dissipation are distributed over the suction surface. Similarly, the one-dimensional mixing loss distribution function

$$\bar{\zeta}_{\epsilon}(\xi) = \int_{0}^{\eta_{\max}} \bar{\zeta}_{\epsilon}(\xi, \eta)\, \mathrm{d}\eta \tag{3-20}$$

describes how losses due to turbulent dissipation are distributed over the suction surface. While the two-dimensional distributions are more fundamental, the one-dimensional distributions are easier to interpret.

$\bar{\zeta}_{\Phi}(\xi)$ and $\bar{\zeta}_{\epsilon}(\xi)$ are plotted in Fig. 3-26 for $\mathrm{Re}_{\infty} = 25{,}000$. Again, the loss distributions are nondimensionalized by $\bar{Z}$.

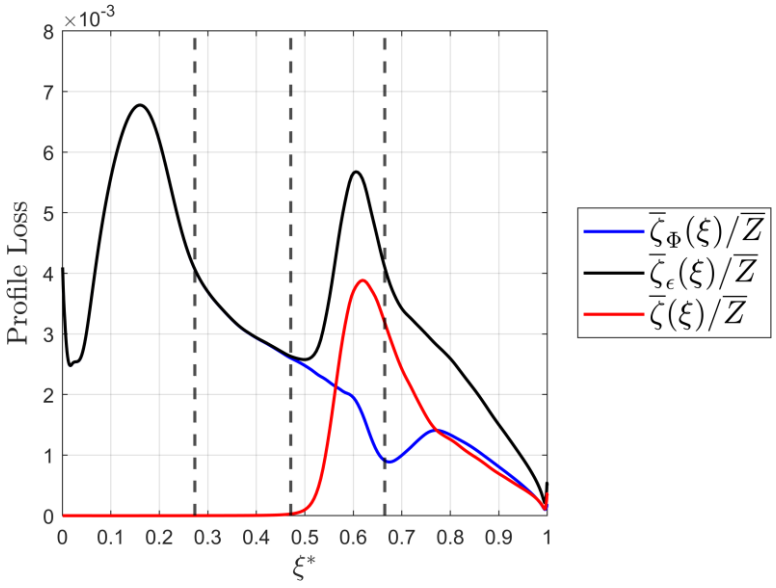

Fig. 3-26: One-dimensional loss distribution functions plotted for $\mathrm{Re}_{\infty} = 25{,}000$.

In Fig. 3-26, $\bar{\zeta}(\xi)$ is the one-dimensional total loss distribution; it is simply the sum of $\bar{\zeta}_{\Phi}(\xi)$ and $\bar{\zeta}_{\epsilon}(\xi)$. Interestingly, $\bar{\zeta}(\xi)$ exhibits two peaks: one before separation and one between transition and reattachment. The first peak in $\bar{\zeta}(\xi)$ occurs in the favorable pressure gradient region upstream of peak suction. In this region, viscous dissipation is the only

source of loss. Thus, the first peak in $\bar{\zeta}(\xi)$ is driven by viscous dissipation. By contrast, the second peak in $\bar{\zeta}(\xi)$ is driven by turbulent dissipation. As the flow transitions, $\bar{\zeta}_\epsilon(\xi)$ increases rapidly. While the intense mixing in the region of transition has the desirable effect of bringing about reattachment, it also contributes significantly to loss. Of the two peaks in $\bar{\zeta}(\xi)$, the first is larger. This is true for all Reynolds numbers and suggests that the largest single source of loss is viscous dissipation in the accelerated, laminar boundary layer upstream of peak suction.

For the majority of the turbulent region (i.e., $\xi > \xi_T$), neither viscous dissipation nor turbulent dissipation is dominant; both contribute roughly equally to $\bar{\zeta}(\xi)$. This is a bit counterintuitive. Naïvely, one might expect *turbulent* dissipation to be dominant in the *turbulent* region—it is in the name after all. However, this is not the case. In fact, the opposite is true. Only for very low Reynolds numbers (e.g., $\mathrm{Re}_\infty = 25{,}000$) does mixing account for the majority of loss in the turbulent region. For most Reynolds numbers, viscous dissipation is the dominant loss generation mechanism in the turbulent region. This raises two interesting questions. What percentage of the loss in the turbulent region is due to viscous dissipation and at what Reynolds number does viscous dissipation become the dominant loss generation mechanism?

Between any two streamwise points (ξ_1 and ξ_2), the fraction of loss due to viscous dissipation is

$$f_\Phi(\xi_1 \to \xi_2) = \frac{\int_{\xi_1}^{\xi_2} \bar{\zeta}_\Phi(\xi)\, d\xi}{\int_{\xi_1}^{\xi_2} \bar{\zeta}(\xi)\, d\xi} \tag{3-21}$$

Similarly, the fraction of loss due to turbulent dissipation is

$$f_\epsilon(\xi_1 \to \xi_2) = \frac{\int_{\xi_1}^{\xi_2} \bar{\zeta}_\epsilon(\xi)\, d\xi}{\int_{\xi_1}^{\xi_2} \bar{\zeta}(\xi)\, d\xi} \tag{3-22}$$

Note that $f_\Phi(\xi_1 \to \xi_2)$ and $f_\epsilon(\xi_1 \to \xi_2)$ are not independent as $f_\Phi(\xi_1 \to \xi_2) + f_\epsilon(\xi_1 \to \xi_2) = 1$. For the turbulent region, $\xi_1 = \xi_T$ and $\xi_2 = \xi_{TE}$. The viscous loss fraction and turbulent loss fraction are plotted as a function of Reynolds number in Fig. 3-27.

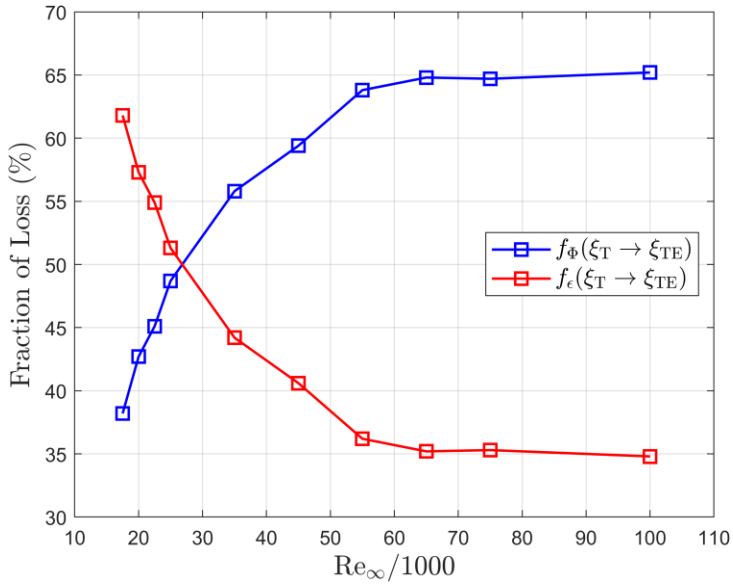

Fig. 3-27: Fraction of loss generated in turbulent region due to viscous dissipation (blue line) and turbulent dissipation (red line).

For $\mathrm{Re}_\infty < 30{,}000$, the mixing loss fraction is significantly greater than viscous loss fraction. At such low Reynolds numbers, the majority of loss comes in the form of mixing in the wake region of the turbulent boundary layer. There is comparatively little loss generated in the inner layer of the turbulent boundary layer because 1) the turbulent region is short owing to the proximity of reattachment to the trailing edge and 2) the velocity gradient across the inner layer is small (see Fig. 3-10). As Reynolds number increases, this trend quickly reverses. For higher Reynolds numbers, the majority of loss comes in the form of viscous dissipation in the inner layer of the turbulent boundary layer. By $\mathrm{Re}_\infty \approx 65{,}000$, approximately two-thirds of the total profile loss generated over the

turbulent region is viscous in nature. Interestingly, the viscous loss fraction remains approximately constant at 66% for $\mathrm{Re}_\infty > 65{,}000$.

It is only natural to wonder how much of the total loss is generated in the turbulent region. The fraction of the total loss generated between any two streamwise points (ξ_1 and ξ_2) is

$$f(\xi_1 \to \xi_2) = \frac{\int_{\xi_1}^{\xi_2} \bar{\zeta}(\xi)\, d\xi}{\int_{\xi_{\mathrm{LE}}}^{\xi_{\mathrm{TE}}} \bar{\zeta}(\xi)\, d\xi} \tag{3-23}$$

$f(\xi_{\mathrm{LE}} \to \xi_{\mathrm{t}})$ and $f(\xi_{\mathrm{T}} \to \xi_{\mathrm{TE}})$ are plotted in Fig. 3-28 as a function of Reynolds number. $f(\xi_{\mathrm{LE}} \to \xi_{\mathrm{t}})$ is the fraction of the total loss generated in the laminar region and $f(\xi_{\mathrm{T}} \to \xi_{\mathrm{TE}})$ is the fraction of the total loss generated in the turbulent region. $f(\xi_{\mathrm{t}} \to \xi_{\mathrm{T}})$ (i.e., the fraction of the total loss generated over the transitional region) is not depicted as it remains approximately constant at 10% across the entire range of Reynolds numbers.

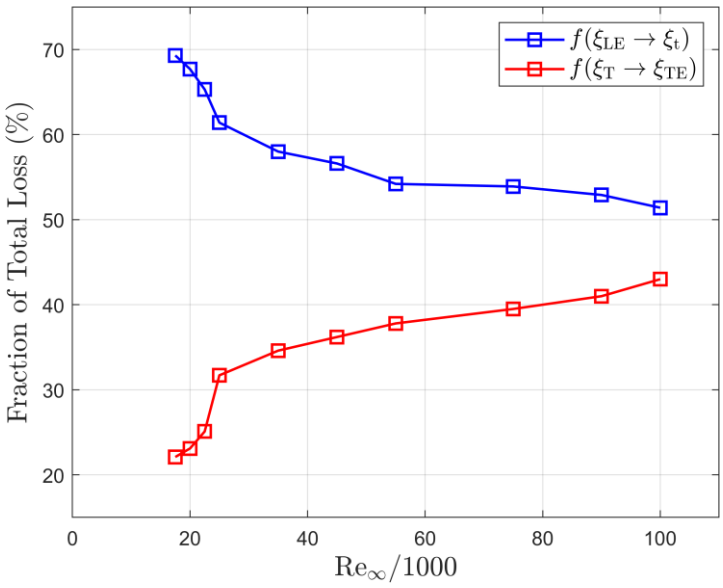

Fig. 3-28: Fraction of total loss generated over the laminar region (blue line) and over the turbulent region (red line).

For $\mathrm{Re}_\infty < 30{,}000$, the vast majority of loss is generated in the laminar region. Of course, this is because the boundary layer is laminar for the majority of the length of the suction surface at these low Reynolds numbers. As Reynolds number increases, the transition point shifts upstream (see Fig. 3-13). Consequently, $f(\xi_\mathrm{T} \rightarrow \xi_\mathrm{TE})$ increases with increasing Reynolds number. At $\mathrm{Re}_\infty = 15{,}000$, only $\sim 25\%$ of the total loss is generated in the turbulent region. By $\mathrm{Re}_\infty = 100{,}000$, this figure has risen to nearly 50%. For $\mathrm{Re}_\infty > 30{,}000$, $f(\xi_\mathrm{T} \rightarrow \xi_\mathrm{TE})$ increases approximately linearly with Reynolds number. Assuming this trend holds for $\mathrm{Re}_\infty > 100{,}000$, the majority of loss will be generated in the turbulent region by $\mathrm{Re}_\infty \approx 120{,}000$.

To conclude this section, an earlier analysis is revised. Recall, when analyzing the lapse curve, it was discovered that Y scaled approximately with $\mathrm{Re}_\infty^{-1/2}$. From this scaling, it was inferred that viscous dissipation was the dominant loss generation mechanism [68]. By integrating Eqns. (3-19) and (3-20) over the suction surface, it is possible to calculate the relative importance of each loss mechanism (i.e., the fraction of the total loss due to each viscous dissipation and mixing). The relative importance of each loss mechanism is summarized in Fig. 3-29 for $\mathrm{Re}_\infty = 15{,}000$ and $\mathrm{Re}_\infty = 100{,}000$.

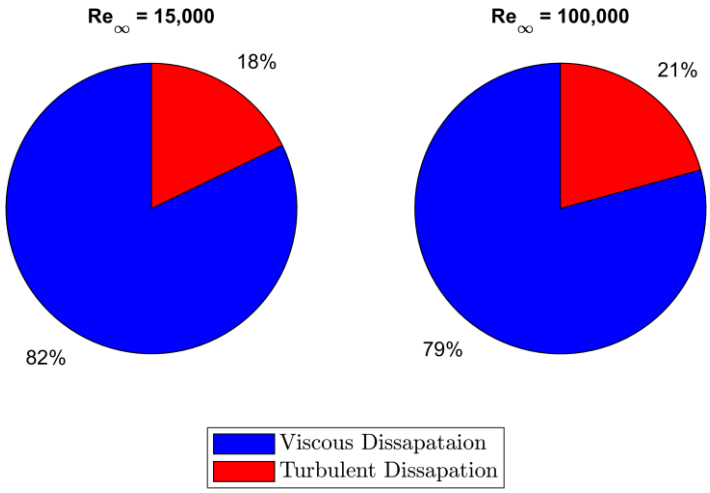

Fig. 3-29: Relative importance of each loss mechanisms for both $\mathrm{Re}_\infty = 15{,}000$ and $\mathrm{Re}_\infty = 100{,}000$.

For both Reynolds numbers, viscous dissipation alone accounts for over 75% of the total loss. Clearly, viscous dissipation is the dominant loss generation mechanism across the range of Reynolds numbers considered. Somewhat surprisingly, turbulent dissipation accounts for approximately 20% of the total loss at both $\mathrm{Re}_\infty = 15{,}000$ and $\mathrm{Re}_\infty = 100{,}000$. As discussed earlier, turbulent dissipation only contributes to loss in the turbulent region (see Fig. 3-26). At $\mathrm{Re}_\infty = 100{,}000$, the boundary layer is turbulent for nearly 60% of the suction surface. At $\mathrm{Re}_\infty = 15{,}000$, the boundary layer is turbulent for only ~25% of the suction surface. Despite the turbulent region being significantly smaller, turbulent dissipation still accounts for roughly the same percentage of the overall loss. This hints at how bursting affects loss.

3.2.3 The Effect of Bursting on Loss Development

Despite the extensive analysis conducted above, it is not clear what effect—if any—bursting has on loss development. Before going any further, it is important to make one point clear: the LSB—in and of itself—is *not* a loss generation mechanism. Only two loss

generation mechanisms are recognized in this study: viscous dissipation and turbulent dissipation. The only way the LSB can affect loss is by influencing either of the aforementioned mechanisms.

Based on Fig. 3-29, it would appear that bursting has the greatest influence on mixing loss. This conclusion is supported by Fig. 3-27. The mixing loss fraction is approximately constant up until bursting, at which point it increases sharply. The opposite is true of the viscous loss fraction. This is somewhat misleading, as it seems to imply that bursting actually decreases viscous loss, which is not the case. What makes Fig. 3-27 a little misleading is the fact that the length of the turbulent region changes with Reynolds number (see Fig. 3-13). The viscous loss fraction and mixing loss fraction are plotted again in Fig. 3-30, except this time they are normalized by the length of the turbulent region:

$$L_T = \xi_{\mathrm{TE}} - \xi_{\mathrm{T}} \tag{3-24}$$

Eq. (3-23) can be made nondimensional by dividing by L_{ss}:

$$L_T^* = \xi_{\mathrm{TE}}^* - \xi_{\mathrm{T}}^* = 1 - \xi_{\mathrm{T}}^* \tag{3-25}$$

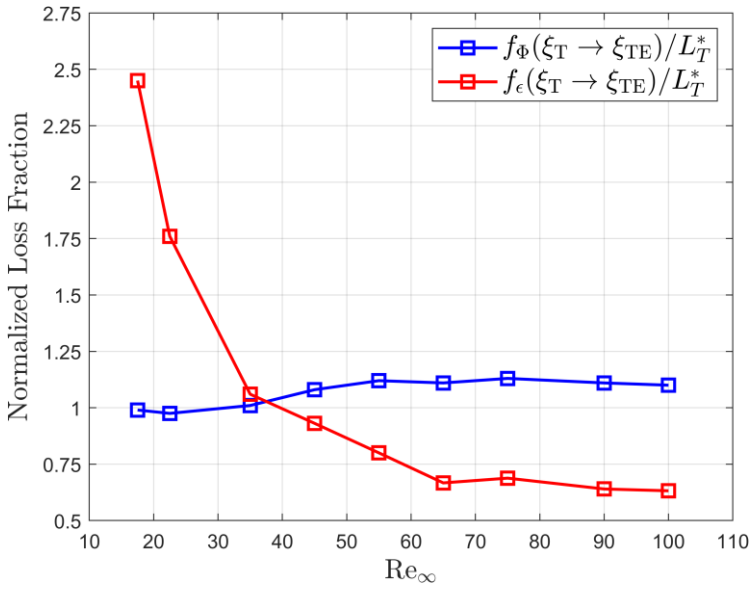

Fig. 3-30: Normalized viscous loss fraction and mixing loss fraction plotted as a function of Reynolds number.

Unlike the viscous loss fraction, the normalized viscous loss fraction is approximately constant over the entire range of Reynolds numbers considered. This means viscous loss scales almost perfectly with the length of the turbulent region. Prior to bursting, mixing loss also scales with the length of the turbulent region. However, after bursting, mixing loss no longer scales with the length of the turbulent region. This strongly suggests that bursting acts to increase mixing loss, which is consistent with prior observations.

So, how does bursting increase mixing loss? The most significant way is simply by increasing the thickness of the LSB (i.e., h). Mixing loss is a strong function of h. This is best illustrated in Fig. 3-31. Increasing h also increases the trailing edge loss by thickening the trailing edge boundary layer. Vortex pairing also likely contributes to increased mixing loss; however, this is difficult to demonstrate.

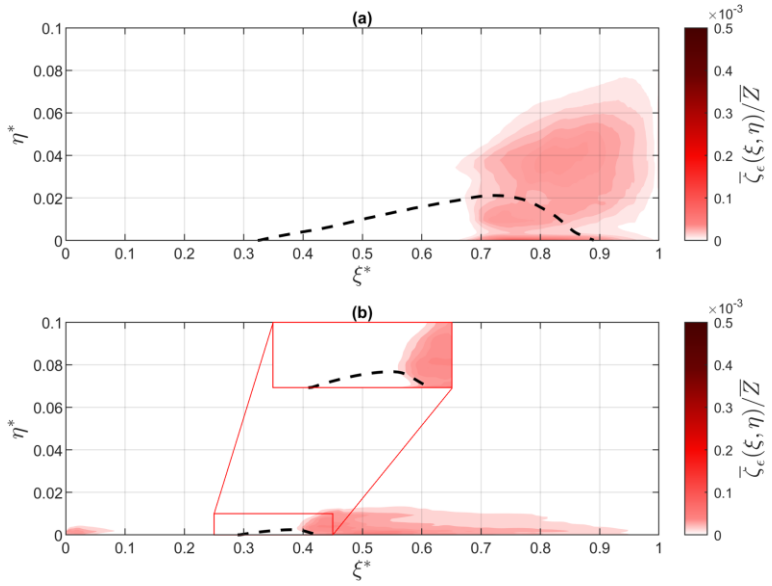

Fig. 3-31: Two-dimensional mixing loss distribution functions for (a) $\mathrm{Re}_\infty = 15{,}000$ and (b) $\mathrm{Re}_\infty = 100{,}000$.

When the LSB is thin (i.e., h is small), mixing is confined to an equally thin region near the suction surface. When the LSB is thick, mixing occurs over a much larger region. Clearly, h is an important parameter in determining how an LSB influences mixing loss.

While not necessarily germane to the current discussion, it is interesting to note that mixing loss is generated within the separation bubble for $\mathrm{Re}_\infty = 15{,}000$ but not for $\mathrm{Re}_\infty = 100{,}000$. This reflects the fact that transition completion occurs upstream of reattachment for long LSBs but not for short LSBs. For short LSBs, transition completion is approximately coincident with the location of reattachment (see Fig. 3-15).

3.2.4 Section Summary

In this section, it was shown that the major source of loss is viscous dissipation. It accounts for over three quarters of the total profile loss across the entire range of Reynolds numbers considered. This is consistent with the fact that the lapse curve scaled with $\mathrm{Re}_\infty^{-1/2}$. The majority of viscous loss is generated in the laminar, accelerated boundary layer

upstream of peak suction. Viscous loss is largely unaffected by bursting. The major way in which bursting affects loss is by increasing the thickness of the LSB which, in turn, increases the mixing loss in the region downstream of reattachment and increases the trailing edge loss by thickening the trailing edge boundary layer.

3.3 Demonstration of Machine-Learning-Based Control

3.3.1 Approach

Up until now, this research has focused on bursting and its effects on both the flowfield and the performance of the L3. At this point it is clear that the effects of bursting are non-trivial. That is, long LSBs are not just *longer* versions of short LSBs. They are phenomena unto themselves, distinct from short LSBs in terms of their vortex dynamics, profile loss footprint, time-averaged topology, etc. To punctuate this study, it is demonstrated how these differences can be leveraged to reduce the energy requirements of steady VGS.

Relative to pulsed VGJs, steady VGJs require significantly more energy to be effective but are more realistic to implement in actual application [3]. The idea of this approach is simple: activate the VGJs less. Obviously, less activation means less energy consumption. The question becomes, how can the VGJs be activated less while maintaining roughly the same effectiveness?

Usually, the objective of activation is to reduce the length of the LSB as much as possible. While simple, this strategy ignores the differences between short and long LSBs. Relative to short LSBs, long LSBs are associated with higher losses, as demonstrated earlier. While decreasing the size (especially the height) of an LSB, in and of itself, does

tend to decrease loss, it also tends to increase the length of the turbulent reattachment region [39]. Since turbulent boundary layers are associated with increased frictional losses, the net result of these competing effects is not always immediately obvious. According to both Mayle [35] and Volino [34], short LSBs are an effective means to induce transition without producing an unnecessarily long turbulent reattachment region. In this sense, short LSBs are optimal. In light of the above discussion, this work proposes that, to maximize efficiency, the objective of activation should depend on whether the LSB is short or long.

Two different control strategies are investigated. In strategy A, VGJ activation is independent of LSB type. The objective of activation is to reduce the length of the separated region as much as possible. In strategy B, VGJ activation is dependent upon LSB type. If the LSB is short, there is no activation. If the LSB is long, the objective of activation is to force the LSB short without suppressing it altogether. It is hypothesized that, relative to strategy A, strategy B will be similarly effective but require considerably less energy.

Both strategies A and B were realized using a simple proportional feedback controller with constant gain. For strategy A, M was continuously adjusted until either 1) the length of the LSB increased or 2) the total pressure loss increased. For strategy B, M was continuously increased until the LSB was assessed to be short. A schematic of the control loop is depicted in Fig. 3-32.

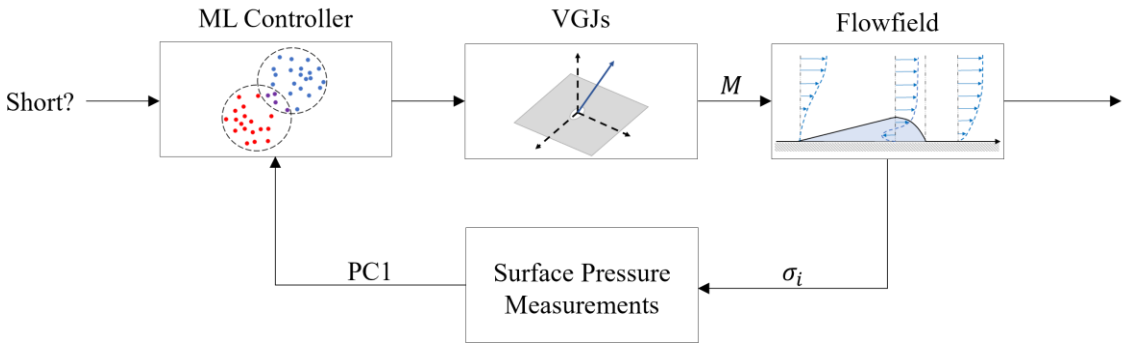

Fig. 3-32: Control loop used for strategy B.

The VGJs were configured exactly as in Sondergaard et al. [16] and, as mentioned earlier, modeled using a simple transpiration boundary condition.

3.3.2 Assessment of Control Strategies

In this section, the performance of strategies A and B are compared for the control of the LSB occurring at $\mathrm{Re}_\infty = 15{,}000$. Note that the LSB is long at this Reynolds number. The goal of this section is to determine what benefit—if any—is afforded by strategy B. Earlier, it was hypothesized that, relative to strategy A, strategy B will be similarly effective but require less energy.

To begin, Y, h, and L are plotted as a function of M in Fig. 3-33. The vertical lines marked M_A and M_B are the cut-off mass ratios for strategies A and B, respectively. M_A is the mass ratio corresponding to the minimum length of the LSB. Note that at $M = M_A$, the LSB was not suppressed entirely. For $M > M_A$, blowing resulted in increased loss; consequently, blowing was cut off at M_A. M_B is the minimum mass ratio required to force the LSB short.

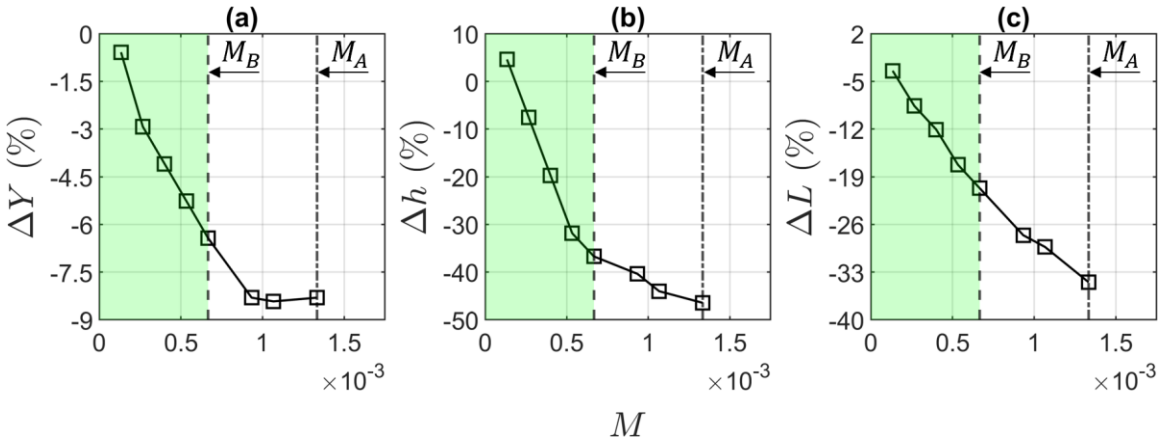

Fig. 3-33: (a) change in total pressure loss coefficient with mass ratio (b) change in the height of the LSB with mass ratio (c) change in the length of LSB with mass ratio.

For $M < 1 \times 10^{-4}$, the VGJs had little to no effect on Y. $M = 1 \times 10^{-4}$ will be referred to as the *cut-in* mass ratio, as it is the minimum mass ratio for which the VGJs had an appreciable effect on performance. Beyond, the cut-in mass ratio, Y decreases approximately linearly with M until $M \approx 1 \times 10^{-3}$, at which point it plateaus. The region over which Y is approximately constant will be referred to as the *plateau region* since there is little change in the benefit of control over this region. Sondergaard et al. [16] reported similar trends in their study of the effect of VGJs on the performance of the Pack-B. Specifically, they found there was a large range of blowing ratios ($1 \leq B \leq 3$)absract over which there was little change in the benefit of control (i.e., Y was constant). The plateau region is significantly shorter in the present study than in the study of Sondergaard et al. [16], ostensibly because the VGJs became detrimental faster. Throughout this analysis, Y is the primary metric used to gauge the benefit of the VGJs.

One of the key takeaways from Fig. 3-33 is that it was possible to force the LSB short without suppressing it entirely. The question is, was there any benefit in doing this? At the machine learning control point (i.e., M_B), Y was reduced by approximately 6.5%, h was reduced by nearly 40%, and L was reduced by approximately 20%. At M_A, Y was

reduced by a little over 8%, h was reduced by approximately 50%, and L was reduced by over 30%. At first, it might seem that the more traditional control strategy is better, as it resulted in larger decreases in Y, h, and L. However, M_A is twice as large as M_B. In increasing M from M_A to M_B, Y decreases by roughly two percentage points. While this is a somewhat sizeable decrease in Y, it doesn't justify the twofold increase in energy expenditure.

Clearly, there is a substantial benefit to strategy B. In light of Fig. 3-33, this should come as no surprise. There is little benefit to increasing the mass ratio beyond $M \approx 1 \times 10^{-3}$. This corresponds to the point at which Y first begins to plateau. Sondergaard et al. [18] dubbed this point the *minimum effective blowing ratio* (equivalently, the minimum effective mass ratio). In the ensuing discussion, it is assumed that the minimum effective mass ratio (M_{opt}) is to the optimum operating point.

To a good first approximation, $M_B \approx M_{\text{opt}}$, as there is only a small difference in performance between the two operating points. The machine-learning-based controller was previously shown to be a bit conservative; consequently, it likely cut off blowing prematurely. Recall, the model identified bursting as occurring over the range $40{,}000 \leq \text{Re}_\infty \leq 65{,}000$. While the upper bound of this range is correct, the lower bound is a little conservative. In reality, bursting occurs over the range $55{,}000 \leq \text{Re}_\infty \leq 65{,}000$. If the hyperparameters of the machine learning model (specifically, the so-called *fuzzifier*) were better tuned, it is possible M_B would be closer to M_{opt}. That being said, there is no reason that M_B should equal M_{opt} as they correspond to different control objectives. M_B is the minimum mass ratio required to force the LSB short; M_{opt} is the mass ratio required to

minimize total pressure loss. The fact that M_B is close to M_{opt} suggests that control strategy B is a good proxy for minimizing total pressure loss.

One of the chief difficulties in effectively applying VGJs lies in determining M_{opt}. In most studies, M_{opt} (or B_{opt}) is determined using Y. However, it is not practical to base a controller on Y. The results of this study suggest that, for the control of an LSB, M_{opt} can be roughly approximated as M_B. This is beneficial because M_B can be determined using the machine learning model outlined in this study which requires only a few pressure measurements. It is certainly more feasible to base a controller on pressure than on Y. Remember, the overarching goal of this work is to increase the feasibility of VGJs.

Another key takeaway from Fig. 3-33 is that Y trends more closely with h than l. Much like Y, h decreases rapidly between the cut-in mass ratio and M_{opt}. Beyond M_{opt}, h still decreases, but at a much shallower rate. l decreases almost linearly with M. The fact that Y trends with h and not l suggest that, between the two length scales, h is more indicative of how the LSB affects performance. This echoes the conclusions drawn earlier regarding how bursting affects loss. More than likely, the main way in which the VGJs decreased loss was by decreasing the thickness of the LSB, thereby decreasing the mixing loss generated in the region downstream of reattachment. This conclusion is supported by Fig. 3-31. It is difficult to apply the same type of loss analysis used before, as the flow is now fully three-dimensional. To perform an in-depth loss analysis on the three-dimensional flowfield is outside the scope of the current work and is likely a study unto itself, requiring new methods of analysis and visualization.

Chapter 4: Conclusions

This section is organized as follows. First, the guiding research objectives are revisited and conclusions pertaining to each objective are presented. Then, recommendations for future work are given.

4.1 Research Objective 1

Research Objective 1: *show that the LSB bursts over a critical range of Reynolds numbers*.

It was conclusively shown that bursting occurred over the range $55{,}000 \leq \mathrm{Re}_{\infty} \leq 65{,}000$. Bursting was accompanied by a dramatic increase in both the length and height of the LSB. The length of the LSB increased not because the separation point changed but because the reattachment point changed. Upon bursting, the reattachment point abruptly shifted downstream. The separation point remained approximately constant through bursting. While bursting significantly affected the reattachment point, it had no effect on the transition onset or transition completion point. This supports the theory that bursting is independent of the transition process and occurs as a result of a sudden failure of the shear layer to reattach [27,29]. For long LSBs, transition completion occurred upstream (in some cases, as much as $\sim 0.2 L_{\mathrm{ss}}$) of the location of time-averaged reattachment. For short LSBs,

transition completion was approximately coincident with the location of time-averaged reattachment.

4.2 Research Objective 2

Research Objective 2: *develop a machine-learned bursting criterion and assess its ability to predict bursting*.

A novel cluster-based bursting criterion was developed. Given three pressure measurements taken in the neighborhood of peak suction, the trained model returned the likelihood (i.e., probability) that the LSB was long and/or short. Relative to existing bursting criteria, the present model shows its utility in two ways. First, it requires only a few pressure measurements. Pressure is easy to measure, especially relative to quantities such as θ or h. Second, the present model is probabilistic rather than deterministic. As Gaster [31] himself acknowledged, bursting is not an instantaneous phenomenon; it occurs over a finite range of Reynolds numbers (or angles of attack). During bursting, an LSB is neither short, nor long; it exists in a sort of "gray" area between the two states. All currently existing models are deterministic. They recognize only two states: short and long. The present model recognizes a continuum of states. Instead of being either short or long, it allows an LSB to be 60% short and 40% long or 90% short and 10% long. In this manner, the present model is more consistent with reality, as bursting is a continuous phenomenon. While the present model performed well in this work, it likely needs significantly more training data—from a diversity of applications—to perform well in general. With that said, it certainly shows promise.

4.3 Research Objective 3

Research Objective 3: *determine how bursting affects the time-averaged topology, vortex dynamics, and loss footprint of the separation bubble*

It was found that, for short LSBs, vortex shedding proceeded in the usual manner. For long LSBs, vortex pairing was observed to occur. A strong correlation between long LSBs and vortex pairing was established. Vortex pairing is the process whereby two neighboring spanwise vortices interact to produce a third vortex of opposite sign. Vortex pairing caused small, counter-rotating vortices to be periodically ejected into the shear layer. This process altered the time-averaged topology of the LSB to include a second, counter-rotating vortex located beneath the reverse-flow vortex. Since the counter-rotating vortex produced by vortex pairing displaced the reversed-flow vortex, it is possible that the onset of vortex pairing is what drives the rapid increase in h observed at bursting. However, further study is needed to ascertain this.

In regard to loss, it was shown that the major source of loss was viscous dissipation. Viscous dissipation accounted for over three quarters of the total profile loss across the entire range of Reynolds numbers considered. This was consistent with the fact that the lapse curve scaled with $\mathrm{Re}_{\infty}^{-1/2}$ [68]. Viscous loss was largely unaffected by bursting. The major way in which bursting affected loss was by increasing the thickness of the LSB which, in turn, increased the mixing loss in the region downstream of reattachment and increased the trailing edge loss by thickening the trailing edge boundary layer.

4.4 Research Objective 4

Research Objective 4: *demonstrate how, with the aid of a machine-learned bursting criterion, the differences between long and short LSBs might be leveraged to reduce the energy requirements of steady VGJs*

It was proposed that, to maximize efficiency, VGJ actuation should depend upon whether the LSB is short or long. To explore this idea, two control strategies were tested. In the first control strategy (henceforth, strategy A), actuation was independent of LSB type. In the second control strategy (henceforth, strategy B), actuation was dependent upon LSB type. The VGJs were actuated only to the extent that the LSB was forced short, but not suppressed entirely. Both control strategies were tested on the L3 at a Reynolds number of 15,000. At this Reynolds number the LSB was long. A simple proportional feedback controller with constant gain was used to realize both control strategies.

First and foremost, it was demonstrated that it was, in fact, possible to force the LSB short without suppressing it entirely. At the onset of this study, it was not immediately clear whether this would be a feasible control objective given that it relied on such subtle differences in flow physics. However, it proved possible.

Strategy B performed similar to strategy A but required half the energy input. Using strategy A, the total pressure loss coefficient was reduced by a little over 8%. Using strategy B, the total pressure loss coefficient was reduced by ~6.5%. While strategy A resulted in a greater reduction in the total pressure loss coefficient, it required significantly more energy. The optimum mass ratio (M_{opt}) was located somewhere between the mass ratio of strategy A (M_A) and strategy B (M_B). If the hyperparameters of the machine

learning model were adjusted, it is possible that M_B would more closely align with M_{opt}, as the machine learning model was somewhat conservative in its identification of busting. That being said, there is no reason that M_B should equal M_{opt} as they correspond to different control objectives. M_B is the minimum mass ratio required to force the LSB short; M_{opt} is the mass ratio required to minimize total pressure loss. The fact that M_B is close to M_{opt} suggests that control strategy B is a good proxy for minimizing total pressure loss. This is beneficial because total pressure loss is not easily measured.

4.5 Recommendations for Future Work

A companion experimental study would be useful, particularly for confirming some of the phenomena reported in this research. Specifically, it would make for an excellent experimental study track the vortex develop up to and through bursting to confirm that vortex pairing is, in fact, a characteristic of long LSBs. It would also be beneficial to experimentally investigate the use of a machine-learned bursting criterion for flow control, similar to as was done at the conclusion of this research.

References

[1] Howell, R. J., Hodson, H. P., Schulte, V., Stieger, R. D., Schiffer, H.-P., Haselbach, F., and Harvey, N. W., 2002, "Boundary Layer Development in the BR710 and BR715 LP Turbines— The Implementation of High-Lift and Ultra-High-Lift Concepts," *ASME J. Turbomach.,* 124(3), pp. 385-392.

[2] Schmitz, J. T., Perez, E., Morris, S. C., Corke, T. C., Clark, J. P., Koch, P. J., and Puterbaugh, S. L., 2016, "Highly Loaded Low-Pressure Turbine: Design, Numerical, and Experimental Analysis," *AIAA J. Prop. Power*, 32(1), pp.142-152.

[3] Bons, J., Benton, S., Bernardini, C., and Bloxham, M., 2018, "Active Flow Control for Low-Pressure Turbines," *AIAA J.*, 56(7), pp. 2687-2698.

[4] Curtis, E. M., Hodson, H. P., Banieghbal, M. R., Denton, J. D., Howell, R. J., and Harvey, N. W., 1997, "Development of Blade Profiles for Low-Pressure Turbine Applications," *ASME J. Turbomach.*, 119(3), pp. 531-538.

[5] Ashpis, D., 2002, "The NASA Low Pressure Turbine Flow Physics Program: A Review," *Minnowbrook III: 2000 Workshop on Boundary Layer Transition and Unsteady Aspects of Turbomachinery Flows*, NASA report NO. NASA/CP-2002101352.

[6] Clark, J. P., Paniagua, G., and Cukurel, B., 2023, "On the Development of High Lift High Work Low-Pressure Turbines," *Proceedings of the ASME 2023 Turbo Expo*, Boston, MA, June 26-30, ASME Paper No. GT2023-103164.

[7] Bons, J., Sondergaard, R., and Rivir, R., 1999, "Control of Low-Pressure Turbine Separation Using Vortex Generator Jets," *37th AIAA Aerospace Sciences Meeting and Exhibit*, Reno, NV, January 11-14, AIAA Paper No. AIAA-99-0367.

[8] Praisner, T. J., Grover, E. A., Knezevici, D. C., Popovic, I., Sjolander, S. A., Clark, J. P., and Sondergaard, R., 2013, "Toward the Expansion of Low-Pressure-Turbine Airfoil Design Space," *ASME J. Turbomach.*, 135(6), pp. 061007-1:8.

[9] Volino, R. J., 2011, "Combined Effects of Wakes and Pulsed Vortex Generator Jet Flow Control on Boundary Layer Separation on a Very High Lift Low Pressure Turbine Airfoil," *Proceedings of the ASME 2011 Turbo Expo*, Vancouver, British Columbia, Canada, June 6-10, ASME Paper No. GT2011-46106.

[10] Bons, J. P., Hansen, L. C., Clark, J. P., Koch, P. J., and Sondergaard, R., 2005, "Designing Low-Pressure Turbine Blades with Integrated Flow Control," *Proceedings of the ASME 2005 Turbo Expo,* Reno, NV, June 6-9, ASME Paper No. GT2005-68962.

[11] Flatt, J., 1961, "The History of Boundary Layer Control Research in the United States of America," *Boundary Layer and Flow Control: Its Principles and Applications,* G. Lachmann, ed., Pergamon Press, New York, pp. 122-143.

[12] Gad-el-Hak, M., 1996, "Modern Developments in Flow Control," *ASME J. Appl. Mech. Rev.,* 49(7), pp. 365-389

[13] Johnston, J. P., and Nishi, M., 1990 "Vortex Generator Jets - Means for Flow Separation Control," *AIAA J.,* 28(6), pp. 989-994.

[14] Bons, J. P., Sondergaard, R., and Rivir, R. B., 2002, "The Fluid Dynamics of LPT Blade Separation Control Using Pulsed Jets," *ASME J. Turbomach.,* 124(1), pp., 77-85.

[15] Postl, D., Gross, A., and Fasel, H., 2004, "Numerical Investigation of Active Flow Control for Low-Pressure Turbine Blade Separation," *42nd AIAA Aerospace Sciences Meeting and Exhibit,* Reno, NV, January 5-8, AIAA Paper No. AIAA 2004-750.

[16] Sondergaard, R., Rivir, R. B., and Bons, J. P., 2002, "Control of Low-Pressure Turbine Separation Using Vortex-Generator Jets," *AIAA J. Prop. Power,* 18(4), pp. 889-895.

[17] McQuilling, M., and Jacob, J., 2004, "Effect of Chord Location on Separation Control with Vortex Generator Jets on Low Pressure Turbine Blades," *2nd AIAA Flow Control Conference,* Portland, OR, June 28 – July 1, AIAA Paper No. AIAA 2004-2205.

[18] Sondergaard, R., Bons, J. P., Sucher, M., and Rivir, R. B., 2002, "Reducing Low-Pressure Turbine Stage Blade Count Using Vortex Generator Jet Separation Control," *Proceedings of the ASME 2002 Turbo Expo,* Amsterdam, The Netherlands, June 3-6, ASME Paper No. GT2002-30602.

[19] Brunton, S. L., Noack, B. R., and Koumoutsakos, P., 2020, "Machine Learning for Fluid Mechanics," *Annual Review of Fluid Mechanics,* 52(1), pp. 477-508.

[20] Brunton, S. L., and Noack, B. R. 2015, "Closed-Loop Turbulence Control: Progress and Challenges," *ASME Appl Mech Rev.,* 67(5), pp. 050801:1-48.

[21] Lee, C., Kim, J., Babcock, D., and Goodman, R., 1997, "Application of Neural Networks to Turbulence Control for Drag Reduction," *Physics of Fluids,* 9(6), 1740-1747.

[22] Brehm, C., Gross, A., and Fasel, H., 2006, "Closed-Loop Control of Low-Pressure Turbine Laminar Separation," *3rd Annual Flow Control Conference,* San Francisco, CA, June 5-8, AIAA Paper No. AIAA 2006-3021.

[23] Murphy, K., 2012, *Machine Learning: A Probabilistic Perspective*, MIT Press, Cambridge, MA.

[24] Kaiser, E., Noack, B. R., Spohn, A., Cattafesta, L. N., and Morzyński, M., 2017, "Cluster-Based Control of a Separating Flow over a Smoothly Contoured Ramp," *Theoretical and Computational Fluid Dynamics*, 31(5), pp. 579-593.

[25] Kaiser, E., Noack, B. R., Cordier, L., Spohn, A., Segond, M., Abel, M., Daviller, G., Östh, J., Krajnović, S., and Niven, R. K., 2014, "Cluster-Based Reduced-Order Modelling of a Mixing Layer," *Journal of Fluid Mechanics*, 754, pp. 365-414.

[26] Nair, A. G., Yeh, C.-A., Kaiser, E., Noack, B. R., Brunton, S. L., and Taira, K., 2019, "Cluster-Based Feedback Control of Turbulent Post-Stall Separated Flows," *Journal of Fluid Mechanics*, 875, pp.345-375.

[27] Hatman, A., and Wang, T., 1999, "A Prediction Model for Separated-Flow Transition," *ASME J. Turbomach.*, 121(3), pp. 594-602.

[28] Owen, R., and Klanfer, L., 1953, "On the Laminar Boundary Layer Separation from the Leading Edge of a Thin Airfoil," Royal Aircraft Establishment Report No. Aero. 2508.

[29] Horton, H., P., 1968, "Laminar Separation Bubbles in Two- and Three-Dimensional Incompressible Flow," Ph.D. dissertation, Queen Mary University of London, London, UK.

[30] Tani, I., 1964, "Low-Speed Flows Involving Bubble Separations," *Progress in Aerospace Sciences*, 5, pp. 70-103.

[31] Gaster, M., 1969, "The Structure and Behavior of Laminar Separation Bubbles," Aeronautical Research Council Reports and Memoranda Report No. 3595.

[32] Mitra, A., and Ramesh, O. N., 2019, "New Correlation for the Prediction of Bursting of a Laminar Separation Bubble," *AIAA J.*, 57(4), pp. 1400-1408.

[33] Diwan, S. S., Chetan, S. J., and Ramesh, O. N., 2006, "On the Bursting Criterion for Laminar Separation Bubbles," *Sixth IUTAM Symposium on Laminar-Turbulent Transition*. R. Govindarajan, ed., Springer, New York, pp. 401-407.

[34] Volino, R. J., 2003, "Passive Flow Control on Low-Pressure Turbine Airfoils," *ASME J. Turbomach.*, 125(4), pp. 754-764.

[35] Mayle, R. E., 1991, "The Role of Laminar-Turbulent Transition in Gas Turbine Engines," *Proceedings of the ASME 1991 Turbo Expo*, Orlando, FL, June 3-6, ASME Paper No. 91-GT-261.

[36] Kachanov, Y. S., 1994, "Physical Mechanisms of Laminar-Boundary-Layer Transition," *Annual Review of Fluid Mechanics,* 26(1), pp. 411-482.

[37] McAuliffe, B. R., and Yaras, M. I., "Transition Mechanisms in Separation Bubbles Under Low- and Elevated-Freestream Turbulence," *Journal of Turbomachinery,* Vol. 132, No. 1, 2010. https://doi.org/10.1115/1.2812949

[38] Praisner, T. J., and Clark, J. P., 2007, "Predicting Transition in Turbomachinery—Part I: A Review and New Model Development," *ASME J. Turbomach.,* 129(1), pp. 1-13.

[39] Volino, R. J., 2002, "Separated Flow Transition Under Simulated Low-Pressure Turbine Airfoil Conditions—Part 1: Mean Flow and Turbulence Statistics," *ASME J. Turbomach.,* 124(4), pp. 645-655.

[40] Hourmouziadis, J., 1989, "Aerodynamic Design of Low-Pressure Turbines," *Blading Design for Axial Turbomachines,* AGARD Lecture Series No. 167, AGARD-LS-167.

[41] Praisner, T. J., Grover, E. A., Rice, M. J., and Clark, J. P., 2007, "Predicting Transition in Turbomachinery—Part II: Model Validation and Benchmarking," *ASME J. Turbomach.,* 129(1), pp. 14-22.

[42] Coull, J. D., and Hodson, H. P., 2013, "Blade Loading and Its Application in the Mean-Line Design of Low-Pressure Turbines," *ASME J. Turbomach.,* 135(2), pp. 021-032.

[43] Zweifel, O., "The Spacing of Turbomachine Blading, Especially with Large Angular Deflection," *Brown Boveri Review,* Vol. 32, No. 1, 1945.

[44] Perez, E., Schmitz, J. T., Jaffa, N. A., Jemcov, A., Cameron, J. D., and Morris, S. C., 2019, "Detailed Experimental Measurement and RANS Simulation of a Low-Pressure Turbine With High Lift Blading," *Proceedings of the ASME 2019 Turbo Expo,* Phoenix, AZ, June 17-21, ASME Paper No. GT2019-91820.

[45] Kerestes, J., Marks, C., Clark, J. P., Wolff, M., Ni, R.-H., and Fletcher, N., 2023, "LES Modeling of High-Lift High-Work LPT Blades: Part II-Validation and Application," *Proceedings of the ASME 2023 Turbo Expo,* Boston, MA, June 26-29, ASME Paper No. GT2023-101950.

[46] Ni, R.-H., 1982, "A Multiple-Grid Scheme for Solving the Euler Equations," *AIAA J.,* 20(11), pp. 1565-1571.

[47] Ni, R.-H., and Bogoian, J., 1989, "Prediction of 3D Multi-Stage Turbine Flow Field Using a Multiple-Grid Euler Solver," *27th Aerospace Sciences Meeting and Exhibit,* Reno, NV, January 9-12, AIAA Paper No. AIAA-89-0203.

[48] Ni, M., Ni, R.-H., and Clark, J. P., 2023, "LES Modeling of High-Lift High-Work LP Turbine Profiles: Part I: Approach," *Proceedings of the ASME 2023 Turbo Expo*, Boston, MA, June 26-29, ASME Paper No. GT2023-102625.

[49] Georgiadis, N., Rizzetta, D., and Fureby, C., 2009, "Large-Eddy Simulation: Current Capabilities, Recommended Practices, and Future Research," *AIAA J.*, 48(8), pp. 1772-1784

[50] Hartigan, J., 1975, *Clustering Algorithms*. John Wiley & Sons, Inc., NY.

[51] Gorder, P. F., 2006, "Neural Networks Show New Promise for Machine Vision," *Computing in Science & Engineering*, 8(6), pp.4-8.

[52] Bezdek, J. C., 1981, *Pattern Recognition with Fuzzy Objective Function Algorithms*, Springer US, Boston, MA.

[53] Bezdek, J. C., Ehrlich, R., and Full, W., 1984, "FCM: The Fuzzy c-Means Clustering Algorithm," *Computers & Geosciences*, 10(2), pp. 191-203.

[54] Dunn, J. C., 1973, "A Fuzzy Relative of the ISODATA Process and Its Use in Detecting Compact Well-Separated Clusters," *Journal of Cybernetics*, 3(3), pp. 32-57.

[55] MacQueen, J., 1967, "Some Methods for Classification and Analysis of Multivariate Observations," *Proceedings of the Fifth Berkeley Symposium on Mathematic Statistics and Probability, Volume 1: Statistics*. L. M. Le Cam, and J. Neyman, eds., University of California Press, California, pp. 281-297.

[56] Lloyd, S., 1982, "Least Squares Quantization in PCM," *IEEE Transactions on Information Theory*, 28(2), pp. 129-137.

[57] Gross, A., and Fasel, H., 2005, "Simulation of Active Flow Control for a Low Pressure Turbine Blade Cascade," *43rd AIAA Aerospace Sciences Meeting and Exhibit*, Reno, NV, January 10-13, AIAA Paper No. AIAA 2005-869.

[58] Jolliffe, I., 2002, *Principal Component Analysis, Second Edition*, Springer, NY.

[59] Brunton, S. L., and Kutz, J. N., 2019, *Data-Driven Science and Engineering*, University of Cambridge Press, Cambridge, UK.

[60] Volino, R. J., Schultz, M. P., and Pratt, C. M., 2003, "Conditional Sampling in a Transitional Boundary Layer Under High Freestream Turbulence Conditions," *ASME J. Fluids Eng.*, 125(1), pp. 28-37.

[61] Bons, J. P., Reimann, D., and Bloxham, M., 2008, "Separated Flow Transition on an LP Turbine Blade with Pulsed Flow Control," *ASME J. Turbomach.*, 130(2), pp. 021014:1-8.

[62] Volino, R. J., 2010, "Separated Flow Measurements on a Highly Loaded Low-Pressure Turbine Airfoil," *ASME J. Turbomach*., 132(10), pp. 011007: 1-10.

[63] Volino, R. J., 1998, "Wavelet Analysis of Transitional Flow Data Under High Free-Stream Turbulence Conditions," *Proceedings of the ASME 1998 Turbo Expo*, Stockholm, Sweden, June 2-5, ASME Paper No. 98-GT-209.

[64] Jiang, M., Machiraju, R., and Thompson, D., 2002, "A Novel Approach To Vortex Core Region Detection," *Joint EUROGRAPHICS - IEEE TCVG Symposium on Visualization*.

[65] Denton, J. D., 1993, "The 1993 IGTI Scholar Lecture: Loss Mechanisms in Turbomachines," *Journal of Turbomachinery*, 115(4), pp. 621–656. https://doi.org/10.1115/1.2929299

[66] Issa, R. I., 1995, "Rise of Total Pressure in Frictional Flow," *AIAA Journal*, Vol. 33(4), pp. 772–774. https://doi.org/10.2514/3.12435

[67] Curtis, E. M., Hodson, H. P., Banieghbal, M. R., Denton, J. D., Howell, R. J., and Harvey, N. W., 1997, "Development of Blade Profiles for Low-Pressure Turbine Applications," *Journal of Turbomachinery*, Vol. 119(3), pp. 531–538. https://doi.org/10.1115/1.2841154

[68] Bolinches-Gisbert, M., Robles, D. C., Corral, R., and Gisbert, F., 2020, "Prediction of Reynolds Number Effects on Low-Pressure Turbines Using a High-Order ILES Method," ASME J. Turbomach., 142(3), pp. 031002:1-12. https://doi.org/10.1115/1.4045776

[69] Schlichting, H., "Boudary Layer Theory," McGraw-Hill, New York, 1979.

[70] Dähnert, J., Lyko, C., and Peitsch, D. 2013, "Transition Mechanisms in Laminar Separated Flow Under Simulated Low Pressure Turbine Aerofoil Conditions," ASME J. Turbomach., 135(1), pp. 011007: 1-10.

[71] Pritchard, P., and Mitchell, J., 2015, *Fox and McDonald's Introduction to Fluid Mechanics*. Wiley, NY.

[72] Thwaites, B., 1949, "Approximate Calculation of the Laminar Boundary Layer," *Aeronautical Quarterly*, 1(3), 1949, pp. 245–280. https://doi.org/10.1017/S0001925900000184

[73] Bradshaw, P., and Huang, G. P., 1995, "The Law of the Wall in Turbulent Flow," Proceedings of the Royal Society of London. Series A: Mathematical and Physical Sciences, 451(1941), pp. 165–188. https://doi.org/10.1098/rspa.1995.0122

[74] Alam, M., and Sandham, N. D., 2000, "Direct Numerical Simulation of 'Short' Laminar Separation Bubbles with Turbulent Reattachment," *Journal of Fluid Mechanics*, 410(2000). https://doi.org/10.1017/S0022112099008976

[75] Dhawan, S., and Narasimha, R., 1958, “Some Properties of Boundary Layer Flow during the Transition from Laminar to Turbulent Motion,” *Journal of Fluid Mechanics*, 3(4), pp. 418-436.

[76] Volino, R. J., and Hultgren, L. S, 2001, “Measurements in Separated and Transitional Boundary Layers Under Low-Pressure Turbine Airfoil Conditions,” 123(2), pp. 189-197.

[77] Sharma, O. P., Wells, R. A., Schlinker, R. H., and Bailey, D. A., 1981, “Boundary Layer Development on Turbine Airfoil Suction Surfaces,” *Proceedings of the ASME 1981 Turbo Expo*, Houston, TX, March 9-12, ASME Paper No. 81-GT-204.

[78] McAuliffe, B. R., and Yaras, M. I., 2008, “Numerical Study of Instability Mechanisms Leading to Transition in Separation Bubbles,” *ASME Journal of Turbomachinery*, 130(2). https://doi.org/10.1115/1.2750680

[79] Winant, C. D., and Browand, F. K., 1974, “Vortex Pairing : The Mechanism of Turbulent Mixing-Layer Growth at Moderate Reynolds Number,” *Journal of Fluid Mechanics*, 63(02), pp. 237. https://doi.org/10.1017/S0022112074001121

[80] Hatman, A., and Wang, T., 1998, “Separated-Flow Transition: Part 3 — Primary Modes and Vortex Dynamics,” *Proceedings of the ASME 1998 Turbo Expo*, Stockholm, Sweden, June2-5, ASME Paper No. 98-GT-463. https://doi.org/10.1115/98-GT-463